

High-energy spectra of LTT 1445A and GJ 486 reveal flares and activity

H. Diamond-Lowe¹, G. W. King², A. Youngblood³, A. Brown⁴, W. S. Howard^{5, 19}, J. G. Winters^{6, 7},
D. J. Wilson⁸, K. France^{4, 5, 8}, J. M. Mendonça¹, L. A. Buchhave¹, L. Corrales², L. Kreidberg⁹,
A. A. Medina¹⁰, J. L. Bean¹¹, Z. K. Berta-Thompson⁵, T. M. Evans-Soma^{9, 12}, C. Froning¹³,
G. M. Duvvuri¹⁴, E. M.-R. Kempton¹⁵, Y. Miguel^{16, 17}, J. S. Pineda⁸, and C. Schneider¹⁸

¹ Department of Space Research and Space Technology, Technical University of Denmark, Elektrovej 328, 2800 Kgs. Lyngby, DK
e-mail: hdiamondlowe@space.dtu.dk

² Department of Astronomy, University of Michigan, 1085 S. University Ave., 323 West Hall, Ann Arbor, MI 48109, US

³ Exoplanets and Stellar Astrophysics Lab, NASA Goddard Space Flight Center, Greenbelt, MD 20771, US

⁴ Center for Astrophysics and Space Astronomy, University of Colorado, 389 UCB, Boulder, CO 80309, US

⁵ Department of Astrophysical and Planetary Sciences, University of Colorado, 2000 Colorado Avenue, Boulder, CO 80309, US

⁶ Center for Astrophysics | Harvard & Smithsonian, 60 Garden Street, Cambridge, MA 02138, US

⁷ Bridgewater State University, 131 Summer St., Bridgewater, MA 02325, US

⁸ Laboratory for Atmospheric and Space Physics, 1234 Innovation Drive, Boulder, CO 80303, US

⁹ Max Planck Institute for Astronomy, Königstuhl 17, 69117 Heidelberg, DE

¹⁰ Department of Astronomy, The University of Texas at Austin, Austin, TX 78712, US

¹¹ Department of Astronomy & Astrophysics, University of Chicago, Chicago, IL 60637, US

¹² School of Information and Physical Sciences, University of Newcastle, Callaghan, NSW, AU

¹³ Southwest Research Institute, 6220 Culebra Rd., San Antonio, TX 78238, US

¹⁴ Department of Physics and Astronomy, Vanderbilt University, Nashville, TN 37235, US

¹⁵ Department of Astronomy, University of Maryland, 4296 Stadium Drive, College Park, MD 20742, US

¹⁶ Leiden Observatory, Leiden University, P.O. Box 9513, 2300 RA Leiden, NL

¹⁷ SRON Netherlands Institute for Space Research, Niels Bohrweg 4, 2333 CA Leiden, NL

¹⁸ Hamburger Sternwarte, Gojenbergsweg 112, D-21039, Hamburg, DE

¹⁹ NHFP Sagan Fellow

Received

ABSTRACT

The high-energy radiative output, from the X-ray to the ultraviolet, of exoplanet host stars drives photochemical reactions and mass loss in the upper regions of planetary atmospheres. In order to place constraints on the atmospheric properties of the three closest terrestrial exoplanets transiting M dwarfs, we observe the high-energy spectra of the host stars LTT 1445A and GJ 486 in the X-ray with *XMM-Newton* and *Chandra* and in the ultraviolet with HST/COS and STIS. We combine these observations with estimates of extreme-ultraviolet flux, reconstructions of the Ly α lines, and stellar models at optical and infrared wavelengths to produce panchromatic spectra from 1 Å to 20 μ m for each star. While LTT 1445Ab, LTT 1445Ac, and GJ 486b do not possess primordial hydrogen-dominated atmospheres, we calculate that they are able to retain pure CO₂ atmospheres if starting with 10, 15, and 50% of Earth's total CO₂ budget, respectively, in the presence of their host stars' stellar wind. We use age–activity relationships to place lower limits of 2.2 and 6.6 Gyr on the ages of the host stars LTT 1445A and GJ 486. Despite both LTT 1445A and GJ 486 appearing inactive at optical wavelengths, we detect flares at ultraviolet and X-ray wavelengths for both stars. In particular, GJ 486 exhibits two far-ultraviolet flares with absolute energies of 10^{29.5} and 10^{30.1} erg (equivalent durations of 4357 ± 96 and 19724 ± 169 s) occurring three hours apart. Based on the timing of the observations, we suggest that these high-energy flares are related and indicative of heightened flaring activity that lasts for a period of days, but our interpretations are limited by sparse time-sampling. Consistent high-energy monitoring is needed to determine the duration and extent of high-energy activity on individual M dwarfs and the population as a whole.

Key words. stars: low-mass — stars: flare — stars: activity — ultraviolet: stars — ultraviolet: planetary systems — X-rays: stars

1. Introduction

The Kepler mission (Borucki et al. 2010), which operated from 2009 to 2013, determined that small planets (< 4 R_⊕) are the most abundant in the Galaxy (Fressin et al. 2013; Fulton et al. 2017). The Transiting Exoplanet Survey Satellite (TESS, launched 2018 and continuing to operate; Ricker et al. 2015)

along with ground-based transit and radial velocity facilities detect small planets orbiting our closest stellar neighbors and determine the radii and masses of these worlds (e.g., Mayor et al. 2003; Nutzman & Charbonneau 2008; Quirrenbach et al. 2010; Mahadevan et al. 2010; Cosentino et al. 2012; Gillon et al. 2013; Irwin et al. 2015; Seifahrt et al. 2016; Schwab et al. 2016; Bouchy et al. 2017; Artigau et al. 2014). Now, the *James Webb*

Space Telescope (JWST, launched 2021) is providing unprecedented insight into the atmospheres of small worlds (e.g., [Lustig-Yaeger et al. 2023](#); [Greene et al. 2023](#); [Zieba et al. 2023](#); [Moran et al. 2023](#); [Lim et al. 2023](#); [May et al. 2023](#); [Zhang et al. 2024](#)).

A common thread among all small planets whose atmospheres we are currently able to study with state-of-the-art observatories is that they orbit M dwarfs, a stellar type with masses and radii below $0.6\times$ that of the Sun and effective temperatures below 3900 K. While the small sizes, low masses, and large population of nearby M dwarfs allow for relative ease of small planet detection, their extended pre-main sequence phases, persistent activity and flaring, and high-energy fluxes threaten to permanently alter or destroy the atmospheres of those small planets (e.g., [Segura et al. 2010](#); [Seager & Deming 2010](#); [Teal et al. 2022](#); [Chen et al. 2021](#); [Howard et al. 2023](#)).

Stellar ultraviolet photons drive photochemistry in the upper atmospheres of planets, where remote sensing techniques of exoplanet atmospheres, such as transmission spectroscopy, are most sensitive. The first evidence for photochemistry outside the Solar System was recently detected in the atmosphere of a hot Jupiter ([Tsai et al. 2023](#)), demonstrating the importance of understanding complex photochemical reactions when interpreting planetary atmospheres. The relative proportions of far- to near-UV (FUV=912–1700 Å; NUV=1700–3200 Å) flux are particularly important for determining the balance of molecular species, such as H₂O, CH₄, CO₂, CO, O₂, and O₃, in planetary atmospheres ([Tian et al. 2014](#); [Harman et al. 2015](#); [Rugheimer et al. 2015](#)).

High-energy flux at X-ray (=1–100 Å) and extreme-ultraviolet (EUV=100–912 Å) wavelengths drives atmospheric mass loss and has the potential to completely strip small planets of their primordial atmospheres ([Lopez et al. 2012](#); [Owen & Wu 2017](#)). This process occurs during the highly active saturation phase of young stars on timescales of around 100 Myr ([Lopez & Fortney 2013](#); [Owen & Wu 2013](#)), but mass loss from EUV photons may persist on gigayear timescales ([King & Wheatley 2021](#)), and complete atmospheric stripping can continue out to 10 Gyr with active flaring ([France et al. 2020](#)). Small planets on tight orbits around M dwarfs are also vulnerable to atmospheric stripping by stellar winds ([Cohen et al. 2015](#); [Garraffo et al. 2016, 2017](#)).

Results from the large MUSCLES program demonstrated that M dwarfs that are similar in size, mass, and temperature produce a range of fluxes in the UV, making the scaling of high-energy flux from one M dwarf to another highly uncertain ([France et al. 2016](#); [Youngblood et al. 2017](#); [Melbourne et al. 2020](#)). When determining whether or not a terrestrial planet retains an atmosphere, having the exact high-energy output from its host M dwarf is essential, as is work to determine its high-energy past. In the present work, we provide a snapshot of the UV and X-ray outputs of the two closest M dwarfs known to host transiting terrestrial planets: LTT 1445A and GJ 486. To capture the high-energy spectra of these stars, we use the unique spectral coverage and resolving power of the *Hubble* Space Telescope coupled with X-ray information from *XMM-Newton* and *Chandra*. Both LTT 1445A and GJ 486 are considered to be old, inactive M dwarfs based on their measured rotation periods and optical activity indicators, such as H α and Ca II H & K. However, M dwarfs that are quiet at optical wavelengths are known to flare at higher energies (e.g., [Lloyd et al. 2018](#); [Jackman et al. 2024](#)). A flare from LTT 1445A at X-ray wavelengths has already been reported in [Brown et al. \(2022\)](#).

At the time of writing, there are two known planetary companions orbiting LTT 1445A and one planetary companion orbiting GJ 486 ([Winters et al. 2019](#); [Trifonov et al. 2021](#); [Winters et al. 2022](#); [Caballero et al. 2022](#)). All three planets have masses and radii consistent with terrestrial bulk compositions (Table 1). Ground-based optical transmission spectroscopy of LTT 1445Ab rules out solar-composition atmospheres down to 1 bar of surface pressure ([Diamond-Lowe et al. 2023](#)). Ground-based high-resolution transmission spectroscopy of GJ 486b rules out clear H/He-dominated atmospheres as well as clear 100% water vapor atmospheres ([Ridden-Harper et al. 2023](#)). JWST transmission spectroscopy of GJ 486b rules out much higher mean-molecular-weight atmospheres at 1 bar of surface pressure ([Moran et al. 2023](#)). The same JWST data may suggest a water-rich atmosphere on this planet; however the interpretation of these results is degenerate with the presence of star-spots in the transmission spectrum. Upcoming results from JWST emission spectroscopy (GO 1743, PI Mansfield; and 2807 PI Berta-Thompson) and transmission spectroscopy (GO 2515, PI Batalha) will provide further clues as to the atmospheric status of LTT 1445Ab and GJ 486b. To complete the atmospheric picture of these planets, we need measurements of the high-energy spectra of their host stars to pass into photochemical and mass-loss models. Whether or not these planets have atmospheres, and what those atmospheres or rocky surfaces look like, depends on their high-energy stellar environments ([Louca et al. 2023](#)).

The present paper is laid out as follows: In Sect. 2 we provide information on the observations that go into this work. In Sect. 3 we present the time-series analysis of our data. In Sect. 4 we put all of the measured and estimated fluxes together to build a panchromatic spectrum of our targets. We provide an analysis of detected flares in Sect. 5. We discuss our results pertaining to the planets orbiting LTT 1445A and GJ 486, as well as a discussion of M dwarf ages and activity in Sect. 6. We conclude with Sect. 7. The resulting spectra of LTT 1445A and GJ 486 are available for download as high-level science products (HLSPs) from the [mstarpanspec](#) page¹.

2. Observations

We observed the ultraviolet to optical spectra, from 1065–5700 Å, of the two closest M dwarfs to host transiting terrestrial exoplanets, LTT 1445A and GJ 486. We used a combination of HST/COS and HST/STIS (GO 16722, PI H. Diamond-Lowe and Co-PI G. King; GO 16701, PI A. Youngblood and Co-PI K. France) to make these observations and achieved almost complete spectral coverage from the FUV to the optical.

To capture the FUV (912–1700 Å) we used COS/G130M with a central wavelength of 1222 Å and COS/G160M with a central wavelength of 1533 Å. Using COS/G130M at 1222 Å places the Ly α line in the gap between the A and B segments, which is required as part of the bright object protections for COS. We captured NUV (1700–3200 Å) flux using COS/G230L with a central wavelength of 2950 Å. While COS provides higher sensitivity to key transition region lines in the FUV and NUV, the segment gap in the COS/G230L NUV spectrum is rather large, spanning 2113–2785 Å. To fill in this gap we used STIS/G230L with a central wavelength of 2376 Å. In order to connect the UV spectra to optical spectra, we took a brief observation with STIS/G430L with a central wavelength of 4300 Å.

¹ doi: [10.17909/t9-fqky-7k61](https://doi.org/10.17909/t9-fqky-7k61)

Though Ly α emission makes up about 85% of FUV flux for M dwarfs (France et al. 2016), the bulk of the Ly α line core is absorbed by neutral hydrogen in the interstellar medium before we can observe it. For nearby bright M dwarfs it is possible to reconstruct Ly α flux from the observed red and blue wings of the Ly α line (Youngblood et al. 2016), but for most inactive M dwarfs it is prohibitively expensive to capture enough signal in the the Ly α line wings to perform a reconstruction. Though LTT 1445A and GJ 486 are considered inactive M dwarfs, they are close enough to capture enough Ly α flux in the wings of the Ly α profile to perform the reconstruction. To make these observations we used STIS/G140M with a central wavelength of 1222 Å and a narrow 52×0.2'' slit to avoid geocoronal Ly α contamination, which is prevalent at Ly α wavelengths and would leak into the larger 2.5'' aperture of COS. For both targets we gathered STIS/G140M data over three orbits, combining observations from the GO 16701 and 16722 programs. These observations were inspected separately but combined from the two GO Programs in order to boost S/N for the Ly α reconstruction.

For the highest-energy part of the spectrum, we used X-ray data from *XMM-Newton* and the *Chandra* X-ray Observatory. *Chandra* has the high spatial resolution necessary to separate LTT 1445A from the more active LTT 1445BC binary companion 7'' away. With a PSF of 15'' *XMM-Newton* cannot resolve LTT 1445A from its companion stars. For LTT 1445A we used X-ray measurements from the *Chandra* ACIS-S instrument described in Brown et al. (2022), as well as an additional set of observations taken in 2023 (Obs IDs 23377, PI Brown; 27882, PI Howard).

For GJ 486 we used *XMM-Newton* since it can provide broader spectral coverage in the X-ray. We observed GJ 486 for 30 ks with *XMM-Newton* and the EPIC-pn camera as part of GO 16722 (PI Diamond-Lowe and Co-PI King). The apparent visual magnitude of GJ 486 is faint enough that we used all three EPIC cameras with the thin optical blocking filters and in full frame mode. We also made use of the simultaneous Optical Monitor (OM) observation taken with the UVW1 filter; however there were issues with these data, as outlined in Sect. 5.2. We also obtained *Chandra* HRC-I data for GJ 486 (31.5 ks; Obs IDs 26210, 27799, 27942, PI Youngblood) which provided additional measurements of the quiescent soft-X-ray emission. All these instruments sample similar energy ranges between 0.1 and 10 keV (corresponding to a wavelength range of 1.2–120 Å), with lower energy limits of 0.1, 0.16, and 0.3 keV for *Chandra* HRC-I, *XMM-Newton*, and *Chandra* ACIS respectively. However, the *Chandra* ACIS detector has lost significant sensitivity below 1 keV because of molecular contamination.

No currently operating observatory can capture EUV (100–912 Å) data of our targets; however this wavelength range is critical for estimates of atmospheric escape rates (King & Wheatley 2021). We therefore used a differential emission measure (DEM; Duvvuri et al. 2021) to estimate the EUV flux from LTT 1445A and GJ 486 from measured flux at UV and X-ray wavelengths.

3. Time series of LTT 1445A and GJ 486

All HST data used in this work, with the exception of the STIS/G430L observations, were taken in TIME-TAG mode, meaning that we can turn these observations into time series. We used the `*corrtag*.fits` in the case of COS and `*tag*.fits` files in the case of STIS, which have the time and detector location of each detected photon. We present the resulting time

Table 1. Parameters for the LTT 1445A and GJ 486 systems used in this work

Star	Unit	LTT 1445A		GJ 486
Distance	pc	6.8638 ± 0.0012		8.0791 ± 0.0021
Radius	R_{\odot}	0.265 ^{+0.011} _{-0.010}		0.328 ± 0.011
Mass	M_{\odot}	0.257 ± 0.014		0.323 ± 0.015
T_{eff}	K	3340 ± 150		3340 ± 54
Planet		b	c	b
Radius	R_{\oplus}	1.305 ^{+0.066} _{-0.061}	1.147 ^{+0.055} _{-0.054}	1.305 ^{+0.063} _{-0.067}
Mass	M_{\oplus}	2.87 ^{+0.26} _{-0.25}	1.54 ^{+0.20} _{-0.19}	2.82 ^{+0.11} _{-0.12}
Density	g cm ⁻³	7.1 ^{+1.2} _{-1.1}	5.57 ^{+0.68} _{-0.60}	7.0 ^{+1.2} _{-1.0}
a	AU	0.03813 ^{+0.00068} _{-0.00070}	0.02661 ^{+0.00047} _{-0.00049}	0.01734 ^{+0.00026} _{-0.00027}
T_{eq}	K	424 ± 21	508 ± 25	701 ± 13

Notes. Distance values are from *Gaia* Data Release 3 (Gaia Collaboration et al. 2023), otherwise values for the LTT 1445A system are from Winters et al. (2022) and values for GJ 486 are from Trifonov et al. (2021).

series of LTT 1445A and GJ 486 in Figs. 1 and 2, respectively. Negative counts are due to imperfect background subtraction.

We detected by eye one flare in the LTT 1445A COS/G160M data set and two flares in the GJ 486 COS/G130M data set (shaded regions in Figs. 1 and 2). As in Diamond-Lowe et al. (2021), we used the `costools splittag` and `x1dcorr` functions to create our own x1d files that separate out the flare data from the quiescent data. We combined all x1d quiescent data together to create our panchromatic spectra (Sect. 4). Flare data from multiple flares were not combined; each flare was processed separately to determine flare properties (Sect. 5). We additionally detected what may be a small flare in the LTT 1445A COS/G130M observations (top middle panel of Fig. 1); however our flare analysis (discussed in depth in Sect. 5) did not find the flux to be statistically different from the baseline flux. We did not exclude this data from the spectral analysis.

4. Panchromatic spectra of LTT 1445A and GJ 486

To produce panchromatic spectra of LTT 1445A and GJ 486 we combined HST UV measurements, X-ray measurements from *XMM-Newton* and *Chandra X-ray Observatory*, an estimation of the EUV output using the differential emission measure (DEM) method, a reconstruction of the Ly α line, and an extension of the spectra into the infrared with BT-Settl (CIFIST) models (Allard et al. 2003; Caffau et al. 2011). Following previous works (France et al. 2016; Loyd et al. 2016; Diamond-Lowe et al. 2021, 2022), we outline the steps to producing our panchromatic spectra here. High level science products are available on the `mstarpanspec` page of the MAST archive². In this section we work only with the quiescent data, after having removed the flare data during the time series analysis (Sect. 3). We provide stellar parameters used throughout this work in Table 1.

4.1. Ultraviolet

We directly measured the far- and near-UV output of LTT 1445A and GJ 486 with HST/COS and STIS. Between these two instruments we have almost complete coverage of the UV spectrum, with the exception of the Ly α line and regions contaminated by geocoronal airglow.

² <https://archive.stsci.edu/hlsp/mstarpanspec>

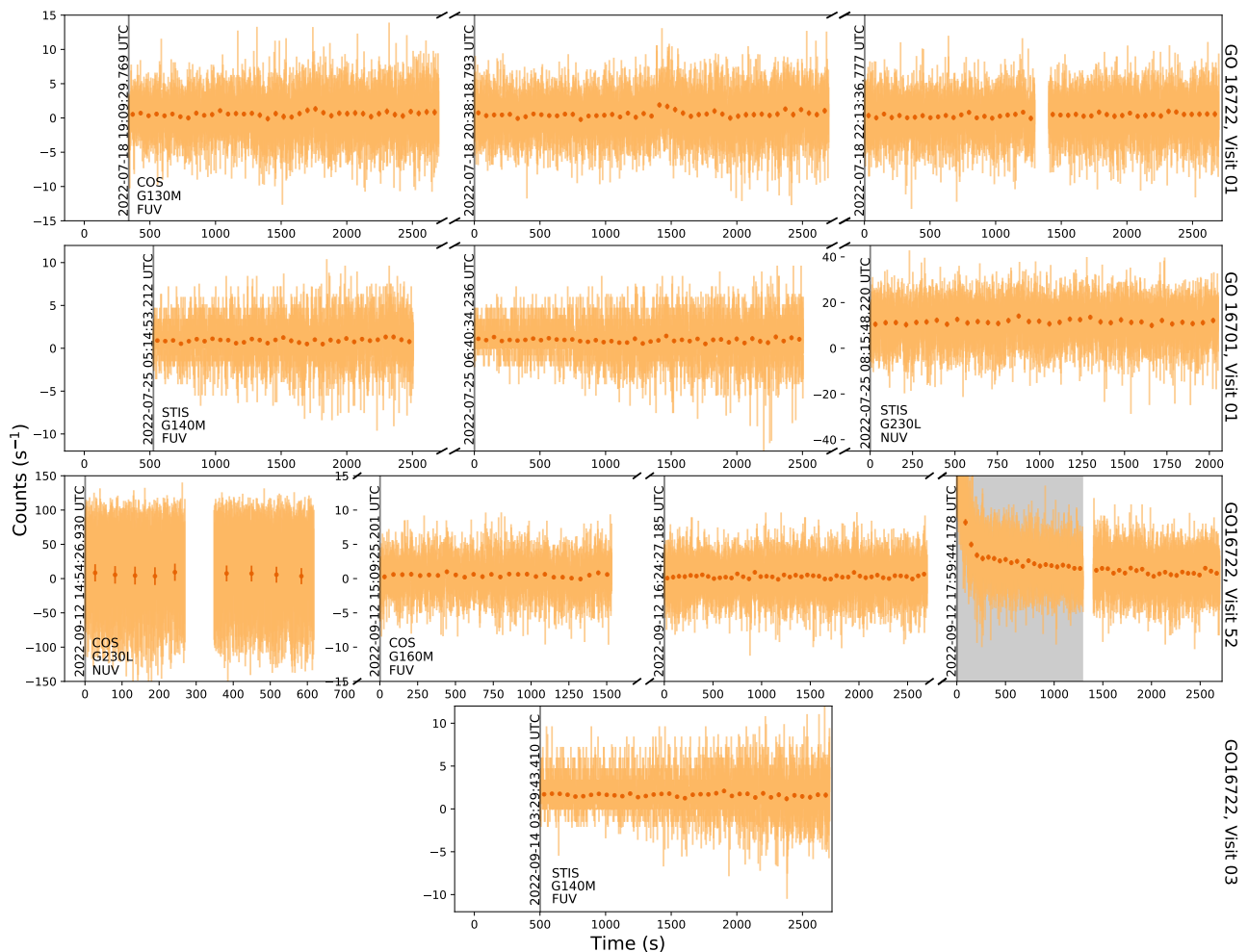


Fig. 1. Time series of LTT 1445A observations used in this analysis from GO Programs 16722 and 16701 (program and visit number specified on right-hand side) presented in chronological order. Count rates are provided in 1 s time bins (light orange) and 1 min time bins (dark orange). The instrument, grating, and detector are given in the first panel of a set of exposures. The shaded gray region shows a flare; these data are excluded from the panchromatic spectrum (Sect. 4) but we analyze the flare data separately in Sect. 5.

Using a list of preidentified geocoronal emission lines³, we identified contamination in our spectra from N I at 1134.980 Å and 1200 Å and from O I at 1302–1307 Å and 1355.6 Å (Feldman et al. 2001). We zeroed-out flux in regions where we identify airglow contamination in the stellar spectra. We note that there are models and tools for modeling and removing contamination from O I airglow lines at 1302–1307 Å (Bourrier et al. 2018; Cruz Aguirre et al. 2023); however we found that modeling and removing the O I contamination can introduce spurious flux into our spectra, while we saw no evidence of underlying stellar spectral features that needed to be preserved.

We measured the flux in prominent UV transition region lines by fitting Voigt models convolved with the COS line spread function (LSF) corresponding to the correct lifetime position for the data to each spectral line. To redefine the LSF from pixels to wavelength we followed instructions in the STScI COS Jupyter notebook on working with COS LSFs⁴. We used the open-source `pyspeckit` (Ginsburg & Mirocha 2011; Ginsburg et al. 2022) to construct the Voigt model, and we estimated uncertainties in the model fit by exploring the parameter space with the open-source `dynesty` nested sampler (Speagle 2020). For blended lines, such

as C III, we fit a combination of Voigt models simultaneously. For lines with well-separated peaks, such as N V, we fit each peak separately, and then summed them for further analysis. We provide a sample of fitted line fluxes in Figs. 3 and 4.

Integrated surface fluxes are provided in Table 2 for LTT 1445A and Table 3 for GJ 486. We computed the surface fluxes as $F_{\text{surf}} = F_{\text{obs}} \times (d/R_s)^2$, where F_{obs} is the integrated observed flux, d is the stellar distance, and R_s is the stellar radius. Values and uncertainties for d and R_s for each target are provided in Table 1. We propagated the uncertainties in d and R_s through to the reported surface fluxes; however the resulting flux uncertainties are dominated by fitting the convolved Voigt profiles to the data.

4.2. Ly α

The core of the Ly α line is attenuated by resonant scattering of neutral hydrogen in the interstellar medium (ISM); however for bright enough stars it is possible to measure the wings of the Ly α profile, and then “reconstruct” the intrinsic Ly α line (Youngblood et al. 2016, 2021, 2022). An alternative method for stars not bright enough to perform the reconstruction is to use known correlations between other UV lines to “estimate” the Ly α flux (Youngblood et al. 2017; Diamond-Lowe et al. 2021,

³ <https://www.stsci.edu/hst/instrumentation/cos/calibration/airglow>

⁴ <https://spacetelescope.github.io/COS-Notebooks/LSF.html>

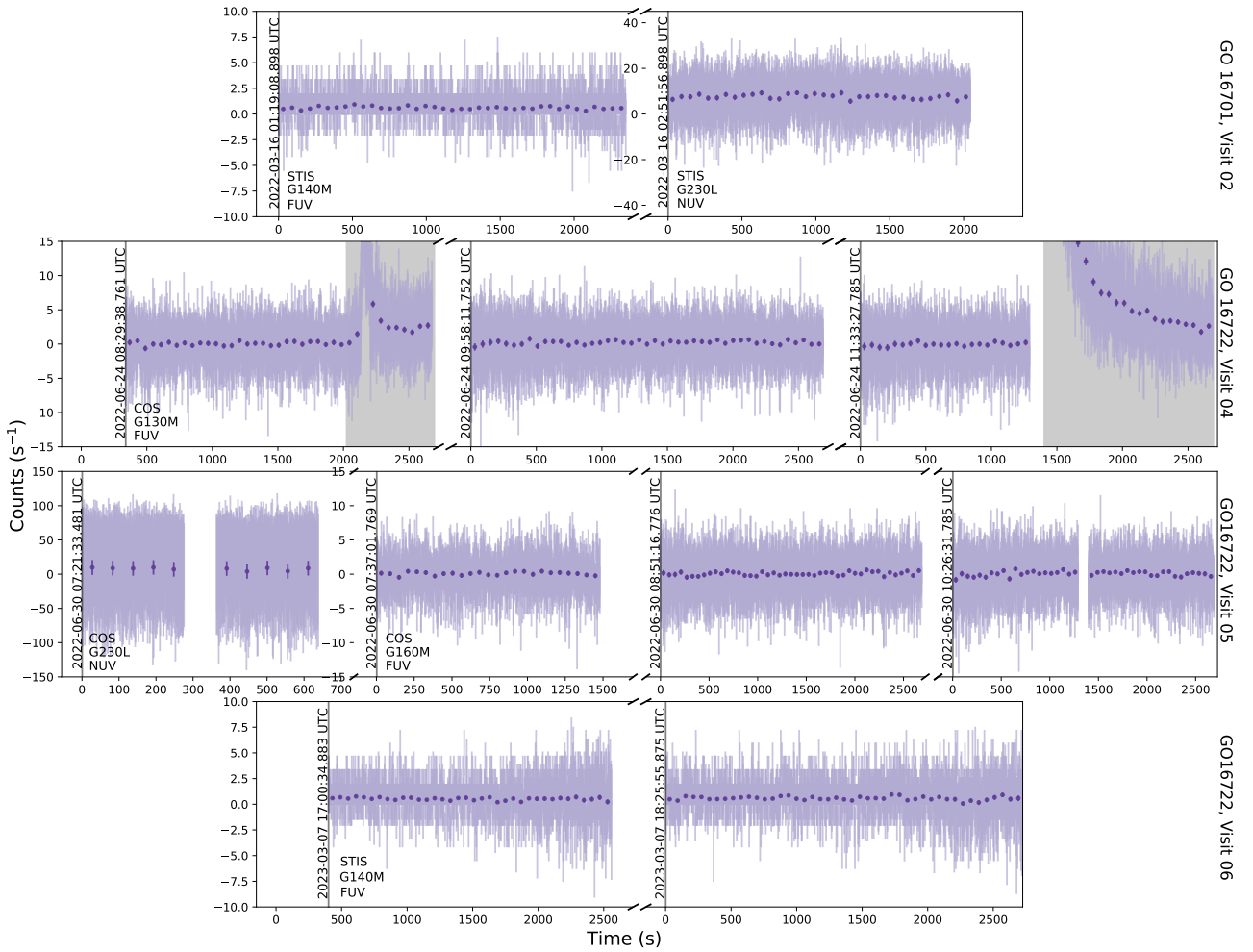


Fig. 2. Same as Fig. 1 but for GJ 486.

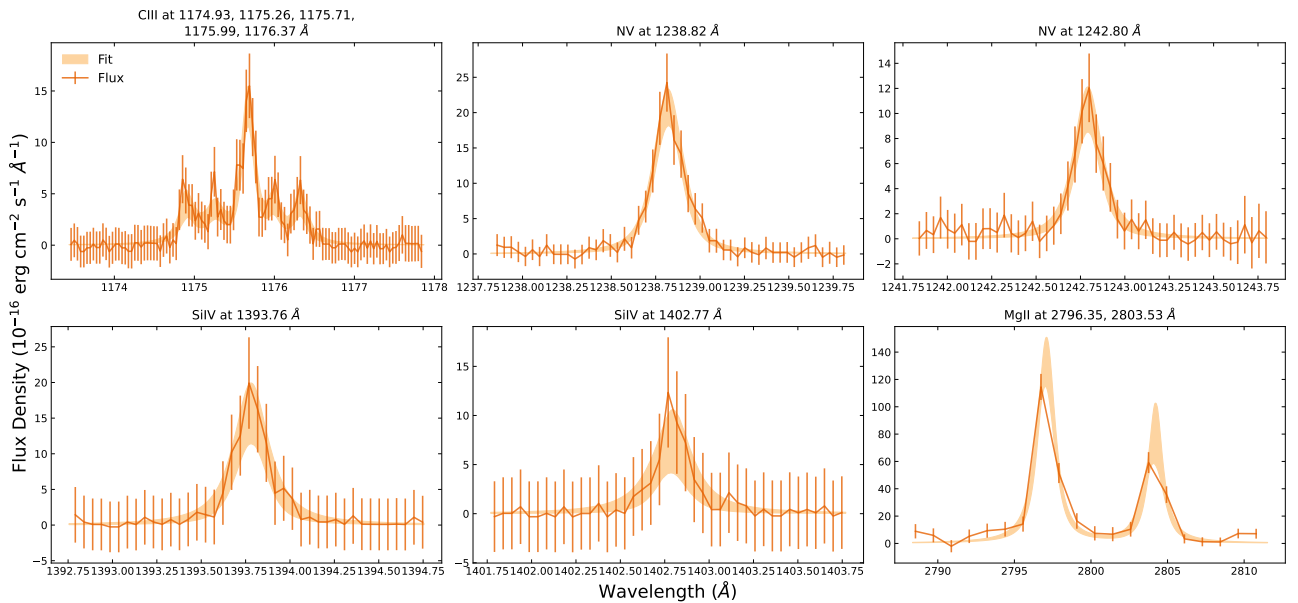


Fig. 3. Sample of measured UV lines with fitted Voigt models for LTT 1445A. The sample covers UV lines from all three COS gratings used (G130M, G160M, and G230L). Lines that are blended, e.g., C III and Mg II, were fit with combined Voigt models, whereas well-separated lines, e.g., N V and Si IV, were fit with individual models. Voigt models are made with `pyspeckit` (Ginsburg et al. 2022) and we explore the model parameter space with `dynesty` (Speagle 2020).

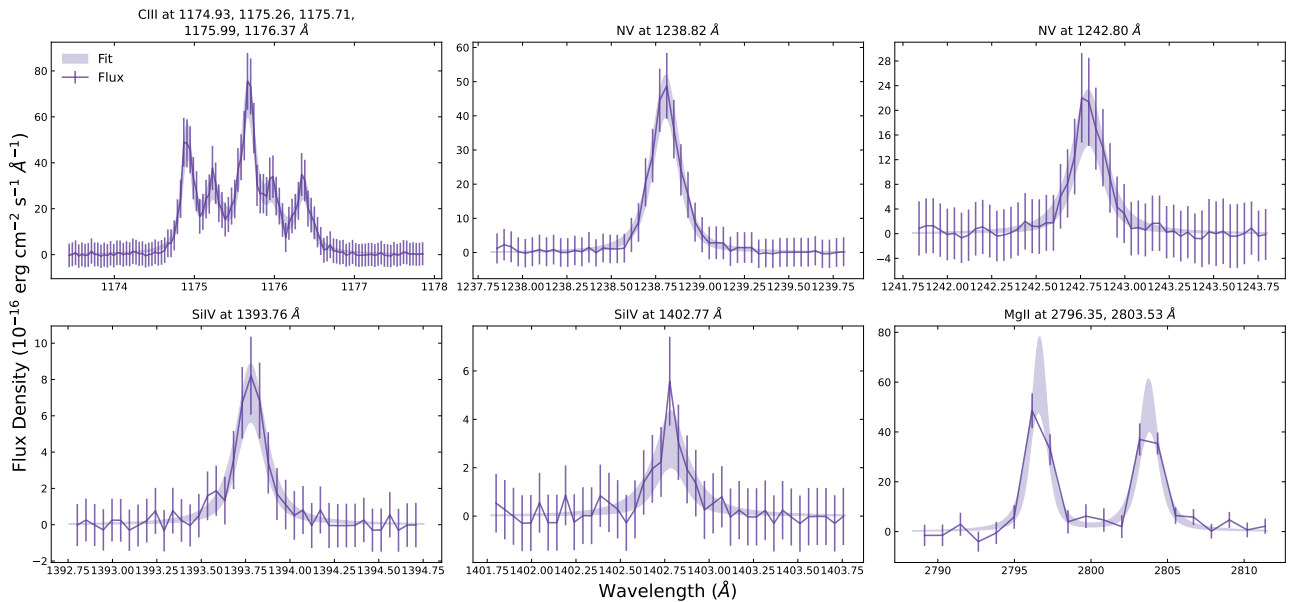


Fig. 4. Same as Fig. 3 but for GJ 486.

Table 2. Measured emission lines from LTT 1445A with HST/COS

	Grating	Total Exposure Time (s)	Line	Line Centers ^a (Å)	$\log_{10}(\text{Surface Flux})^b$ ($\text{erg cm}^{-2} \text{s}^{-1}$)	$\log_{10}(T)^a$
FUV	G130M	7657	C III *	1174.933, 1175.263, 1175.711, 1175.987, 1176.37	2.99 ± 0.12	4.9
			Si III *	1206.555	2.85 ± 0.07	4.8
			N V *	1238.821, 1242.804	2.99 ± 0.06	5.3
			Si II *	1264.738	1.99 ± 0.29	4.5
			C II *	1334.532, 1335.707	3.10 ± 0.06	4.6
	G160M	6830	O V	1371.296	1.73 ± 0.66	5.4
			Si IV *	1393.755, 1402.772	2.95 ± 0.14	4.9
			O IV	1401.163	1.84 ± 0.64	5.1
			C IV *	1548.187, 1550.775	3.61 ± 0.09	5.1
			He II	1640.474	3.20 ± 0.19	4.9
Al II	1670.788	2.89 ± 0.34	4.5			
NUV	G230L	540	Mg II *	2796.350, 2803.531	4.79 ± 0.08	4.2

Notes. Lines marked with an asterisk * are used to compute the DEM function (see Sect. 4.4 and Fig. 11).

^a Values from CHIANTI database v10.1 (Dere et al. 2023)

^b Surface fluxes ($\text{erg cm}^{-2} \text{s}^{-1}$) were calculated by scaling the observed flux by the distance d and stellar radius R_s of LTT 1445A: $F_{\text{Surf}} = F_{\text{Obs}} \times (d/R_s)^2$. For multiple lines, we report the combined surface flux.

2022). LTT 1445A and GJ 486 are both bright enough to do a $\text{Ly}\alpha$ reconstruction, which we used in the panchromatic spectra. We also compared the reconstructed $\text{Ly}\alpha$ flux to the estimated $\text{Ly}\alpha$ flux from UV-UV line correlations.

We combined three STIS/G140M measurements and took a weighted average to build up S/N for the $\text{Ly}\alpha$ reconstruction (Figs. 5 and 6). In the case of LTT 1445A, one of the three observations, from GO 16722 Visit 03, appeared to contain about 1.5 \times the flux of the other two observations; we posit that this additional flux may be associated with the flare that preceded the observation by 48 hours (Fig. 1). A further discussion of prolonged stellar activity can be found in Sect. 6.3.

For comparison, we estimated $\text{Ly}\alpha$ flux for LTT 1445A from UV-UV line correlations found in the MUSCLES sample (Youngblood et al. 2017). In addition to demonstrating the ability

of the UV-UV correlations to recover the data-driven $\text{Ly}\alpha$ reconstruction, this method additionally provides a useful comparison of the UV flux from transition region lines observed with different COS gratings, which cannot be used simultaneously. As demonstrated in Fig. 7, the UV-UV correlation values for $\text{Ly}\alpha$ estimated from individual transition region lines agree well with each other, and the resulting average $\text{Ly}\alpha$ estimate agrees well with the reconstructed $\text{Ly}\alpha$ value. Similar to previous work (e.g., Diamond-Lowe et al. 2022), we conservatively estimated the uncertainty of the individual $\text{Ly}\alpha$ estimates using the rms of the correlations from Youngblood et al. (2017), and took the final estimate as the mean value and the mean uncertainty.

In the case of GJ 486, there is a potential discrepancy between the UV-UV correlation values for $\text{Ly}\alpha$ from transition region lines measured with the COS/G130M grating and those

Table 3. Measured emission lines from GJ 486 with HST/COS

	Grating	Total Exposure Time (s)	Line	Line Centers ^a (Å)	$\log_{10}(\text{Surface Flux})^b$ ($\text{erg cm}^{-2} \text{s}^{-1}$)	$\log_{10}(T)^a$
FUV	G130M	7610	C III *	1174.933, 1175.263, 1175.711, 1175.987, 1176.37	3.8 ± 0.07	4.9
			Si III *	1206.555	3.04 ± 0.08	4.8
			N V *	1238.821, 1242.804	3.27 ± 0.07	5.3
			Si II *	1264.738	2.58 ± 0.24	4.5
			C II *	1334.532, 1335.707	3.71 ± 0.06	4.6
	G160M	6753	O V	1371.296	1.20 ± 0.51	5.4
			Si IV *	1393.755, 1402.772	2.52 ± 0.12	4.9
			O IV	1401.163	1.41 ± 0.54	5.1
			C IV *	1548.187, 1550.775	3.29 ± 0.07	5.1
			He II	1640.474	2.74 ± 0.15	4.9
Al II	1670.788	2.6 ± 0.23	4.5			
NUV	G230L	552	Mg II *	2796.350, 2803.531	4.53 ± 0.08	4.2

Notes. Same as Table 2 but for GJ 486. DEM shown in Fig. 12.

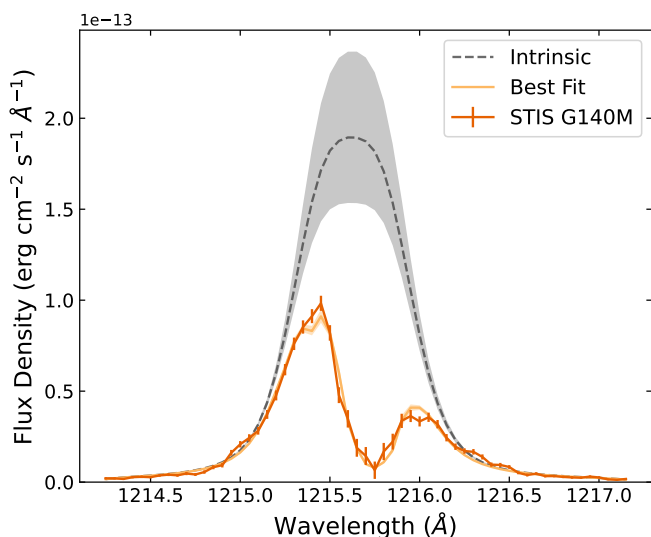


Fig. 5. Reconstruction of the intrinsic Ly α flux of LTT 1445A (gray) using the best fit (light orange) to the measured wings of the Ly α profile observed with STIS/G140M (orange 1σ error bars; Youngblood et al. 2016).

measured with the COS/G160M and G230L gratings (Fig. 8). During observations with the COS/G130M grating we detected two large flares (Fig. 2). These flares are removed from the data and analyzed separately in Sect. 5, but the remaining “quiescent” data may still represent an elevated activity state (more on this in Sect. 6.3). The discrepancy between “quiescent” UV estimates of Ly α suggests that we have not actually observed GJ 486 in true quiescence with the COS/G130M grating. For the purposes of comparison with the Ly α reconstruction, we only used the lines observed with COS/G160M and COS/G230L, which were observed about a week after the COS/G130M observations. The UV-UV correlation values for Ly α estimated from the COS/G160M and G230L lines agree with the Ly α value at the 2σ level.

The reconstructed Ly α profiles for LTT 1445A and GJ 486 are included in the final panchromatic spectrum. Properties de-

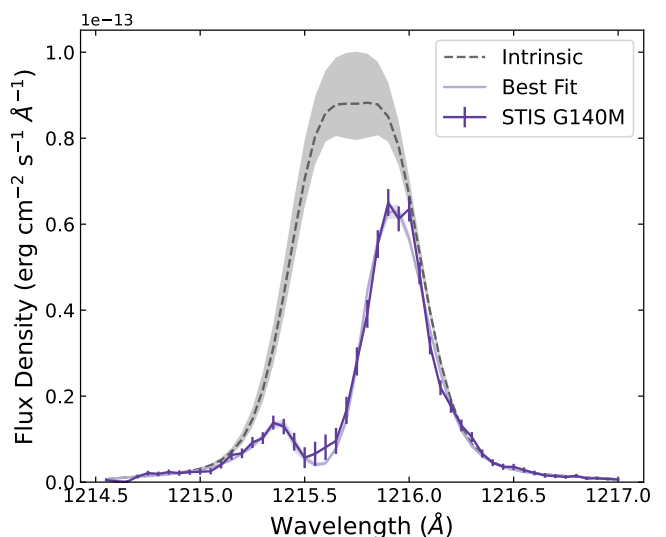


Fig. 6. Same as Fig. 5 but for GJ 486.

rived from the reconstruction are provided in Table 4, along with a comparison to the UV-UV correlation method.

4.3. X-ray

Detecting X-ray flux for most inactive mid-to-late M dwarfs is challenging as their apparent brightness at these wavelengths is typically faint. LTT 1445A and GJ 486 are close enough that X-ray detections are possible. We used *Chandra* to measure X-ray flux from LTT 1445A and both *Chandra* and *XMM-Newton* to measure X-ray flux from GJ 486. We detected X-ray flares for both stars, which are discussed in more detail in Sect. 5. Similar to the UV data, we removed the flare points from the time-series X-ray data to measure quiescent X-ray flux levels. The quiescent X-ray flux measurements were used to construct the panchromatic spectra and inform the DEM estimate of the EUV (Sect. 4.4). Quiescent and flare values from the X-ray observations are provided in Tables 5 and 6 for LTT 1445A and GJ 486, respectively.

Table 4. Ly α values for LTT 1445A and GJ 486

	LTT 1445A	GJ 486
	Reconstruction from STIS/G140M	
$\log_{10}(\text{Surface Flux})$ (erg/cm ² /s)	5.27 ^{+0.08} _{-0.06}	4.88 ^{+0.04} _{-0.03}
$\log_{10}(\text{N(H I)})$ (cm ⁻²)	17.8 \pm 0.1	17.8 \pm 0.1
H I radial velocity (km/s)	13.2 ^{+3.4} _{-2.8}	-18.1 ^{+1.3} _{-2.0}
	Estimate from UV-UV Correlations	
$\log_{10}(\text{Surface Flux})$ from Si III (erg/cm ² /s)	5.37 \pm 0.23	5.48 \pm 0.23
$\log_{10}(\text{Surface Flux})$ from N V (erg/cm ² /s)	5.30 \pm 0.35	5.49 \pm 0.35
$\log_{10}(\text{Surface Flux})$ from Si II (erg/cm ² /s)	5.02 \pm 0.30	5.52 \pm 0.30
$\log_{10}(\text{Surface Flux})$ from C II (erg/cm ² /s)	5.48 \pm 0.40	5.84 \pm 0.40
$\log_{10}(\text{Surface Flux})$ from Si IV (erg/cm ² /s)	5.39 \pm 0.38	5.14 \pm 0.38
$\log_{10}(\text{Surface Flux})$ from C IV (erg/cm ² /s)	5.36 \pm 0.32	5.15 \pm 0.32
$\log_{10}(\text{Surface Flux})$ from He II (erg/cm ² /s)	5.47 \pm 0.32	5.23 \pm 0.32
$\log_{10}(\text{Surface Flux})$ from Mg II (erg/cm ² /s)	5.43 \pm 0.19	5.22 \pm 0.19
$\log_{10}(\text{Surface Flux})$ mean (erg/cm ² /s)	5.35 \pm 0.31	5.19 \pm 0.30 ^a

Notes. Log surface fluxes calculated using distances and stellar radii from Table 1.

^a For GJ 486 we find that lines measured with the COS/G130L grating give systematically higher estimates of the Ly α flux. Given that two large flares were removed from the data taken with this grating, it is possible that the transition region lines we measure with COS/G130L are not completely representative of a quiescent state. We therefore report the Ly α estimate from the UV-UV correlations only with lines in the G160M and G230L gratings for LTT 1445A.

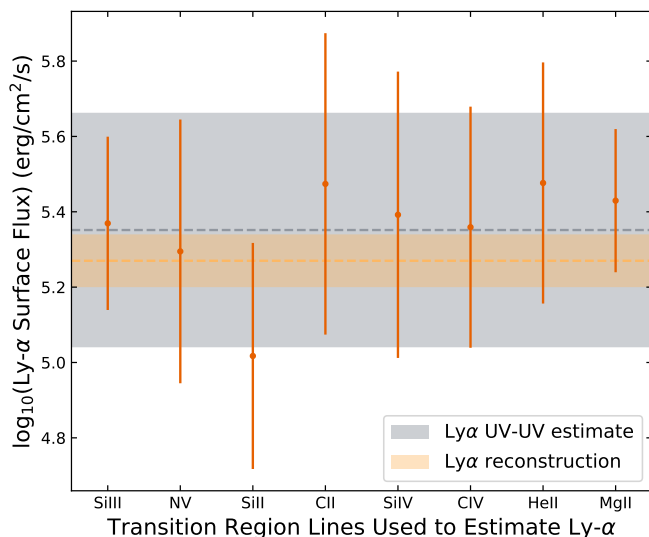


Fig. 7. Deriving the Ly α flux of LTT 1445A using a reconstruction from the wings of the Ly α profile observed with the STIS/G140M grating (orange 1σ band; Youngblood et al. 2016) and using UV-UV line correlations with other measured UV lines with the COS instrument (orange points with 1σ errors, and the average 1σ gray band; Youngblood et al. 2017; Diamond-Lowe et al. 2021, 2022). In the case of LTT 1445A, we find that individual transition region lines agree with each other, and with the reconstructed value.

For LTT 1445A we used *Chandra* observations published in Brown et al. (2022), as well as a new set of observations presented here (Fig. 9, Table 5). The first set of observations, obtained in 2021, distinctly show a flare. An extensive analysis of this flare is reported in Brown et al. (2022) and we do not repeat the process here. We observed LTT 1445A again on 2023 Aug 2 (Obs ID 27882, PI Howard) and did not detect a flare. Estimation of X-ray flux parameters involves spectral fitting using the XSPEC v12.12 software (Arnaud 1996). Count rates were converted to flux values in erg s⁻¹ cm⁻² using the best-fit

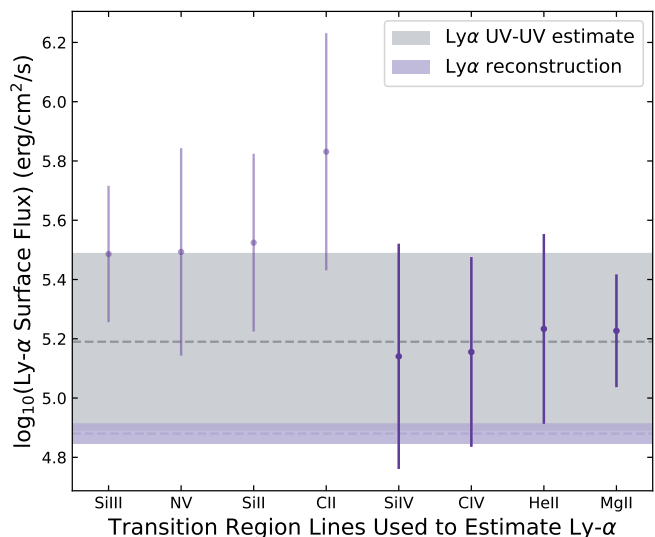


Fig. 8. Same as Fig. 7 but for GJ 486. In this case, we find a discrepancy between the lines observed with COS/G130M and those observed with COS/G160M and COS/G230L. It is possible that this discrepancy is due to the large flares observed during the COS/G130M observations. We only use lines observed with COS/G160M and COS/G230L (darker purple points with 1σ errors) to estimate the Ly α flux with the UV-UV correlation method. The Ly α values from the reconstruction and the UV-UV estimation agree to within 2σ .

single-temperature VAPEC spectrum for an optically thin coronal plasma, assuming a hydrogen column density of 10^{19} cm⁻², subsolar metallicities, and stellar distance provided in Table 1. A full description of how we chose the subsolar abundances can be found in Sect. 4.3 of Brown et al. (2022). We take the 2023 observations as representative of LTT 1445A's typical X-ray state, and divided the flux into three broad spectral bins for use in the DEM (Sect. 4.4). We used only the 2023 observations in the GJ 486 panchromatic spectrum.

For GJ 486 we were able to use *XMM-Newton*, which has better sensitivity at lower energies. We observed GJ 486 for 32 ks on 2021 Dec 23 with the European Photon Imaging Camera (EPIC). A few short periods of high background flaring associated with energetic Solar protons were excluded (Walsh et al. 2014) using the standard processes⁵. Our extracted light curves of GJ 486 are displayed in Fig. 10, with results for three different energy bands: “full” (0.2–2.4 keV), “soft” (0.2–0.65 keV), and “hard” (0.65–2.4 keV). These light curves show evidence of flares, which we describe in more detail in Sect. 5.2.

We extracted separate EPIC-pn spectra for the quiescent epochs of the observation and the biggest flare, which occurred halfway through the time series. The S/N of the second peak was too low to warrant fitting, but this section of the observation was excluded from the quiescent spectrum. We fit the data using a two temperature APEC model, where the temperatures were forced to be the same across the quiescent and flaring spectra, due to the latter only containing five spectral bins. However their respective normalizations are allowed to vary, such that the substantial change in the spectral shape can be accounted for in the fit. We again use the same subsolar abundances from Brown et al. (2022) for these fits, noting that our best fit fixes the Fe abundance, as this parameter becomes unconstrained when allowed to vary. We used C-statistics when performing the fit (Cash 1979). From the best-fit model, we calculated the flux in several broad energy ranges for use in reconstructing the DEM (Sect. 4.4).

We also have observations of GJ 486 using the *Chandra* HRC-I detector obtained on 2023 April 4, July 13, and July 15. These observations appeared to show quiescent emission and the corresponding X-ray luminosity, and we estimated the emission measures assuming a coronal temperature of 0.19 keV (2.2 MK)⁶, because the HRC-I has minimal energy resolution and does not provide a temperature directly.

4.4. Extreme-ultraviolet

There is no currently operating observatory that can detect EUV (100–912Å) flux from LTT 1445A and GJ 486. Energetic photons approaching 912Å are increasingly absorbed by neutral hydrogen in the ISM, making it nearly impossible to detect photons at 912Å for stars other than the Sun. The Extreme-Ultraviolet Explorer (EUVE; Craig et al. 1997), which functioned from 1992–2001, could measure EUV flux from nearby, highly energetic stars, but neither LTT 1445A nor GJ 486 were observed by this mission. Instead, in order to estimate the EUV flux from LTT 1445A and GJ 486, we leveraged the measured transition lines we detect in the UV, as well as the X-ray measurements, in order to construct a DEM function for our targets.

The DEM method takes advantage of the fact that a smoothly varying function with respect to temperature can be fit to the DEMs calculated for observed emission lines in the data; the fitted function can then be used to back out the flux we should measure from emission lines where no data are available, such as those at EUV wavelengths. There are many examples of DEM applications in stellar astrophysics (e.g., Kashyap & Drake 1998; Sanz-Forcada et al. 2003). Here we followed the application of the DEM method to cool dwarf stars (Duvvuri et al. 2021), with several examples now available (e.g., Diamond-Lowe et al. 2021, 2022; Wilson et al. 2021; Feinstein et al. 2022; Duvvuri

et al. 2023). The DEM method relies on some assumptions, for example that each temperature component of the stellar atmosphere can be treated as an optically thin plasma in collisional ionization equilibrium. These assumptions limit the DEM method, but without another way to access the EUV spectra of inactive M dwarfs, the DEM method is the current state-of-the-art for estimating EUV flux for our targets. We note that it is also possible to estimate the EUV flux by scaling from the Ly α line (Linsky et al. 2014) or the Si IV and N V lines (France et al. 2018). Diamond-Lowe et al. (2021) found agreement between these scaling methods and the DEM method for the inactive M dwarf LHS 3844. Here we opt for the DEM method because it utilizes measured flux across the UV and X-ray.

Following methods outlined in Duvvuri et al. (2021) and improving upon code developed in Diamond-Lowe et al. (2021) and Diamond-Lowe et al. (2022), we constructed a DEM for LTT 1445A and GJ 486. For each observed UV line and X-ray band we calculated a “local DEM” that is the local average DEM value required to reproduce the observed flux given the method’s assumptions. We used the CHIANTI atomic database v10.1 to retrieve the maximum formation temperature and emissivity contribution functions for each ion (Dere et al. 1997, 2023). For the X-ray bands we used the CHIANTI database to find every ion that emits in each band, and summed their emissivity contribution functions. We used the peak of this summed function to determine a peak formation temperature. The exception is the *Chandra* HRC-I observation for GJ 486, which did not have any energy resolution, so we took the assumed coronal temperature of 2.2MK as the peak formation temperature. We fit a fifth-order Chebyshev polynomial to the local DEMs, and used the dynesty dynamic nested sampler to explore the parameter space within the prior bounds. We set priors on the Chebyshev polynomial coefficients as prescribed in Duvvuri et al. (2021), as well as included the free parameter s to characterize unknown systematic uncertainties. The resulting DEM functions for LTT 1445A and GJ 486 are shown in Figs. 11 and 12, respectively.

We note that because we do not have any measured EUV constraints for our targets, it is likely that the fitted DEM will over-predict the EUV flux (Del Zanna et al. 2002). This over-prediction is nonuniform and therefore cannot be corrected with a simple scaling. Duvvuri et al. (2021) found an overestimation by a factor of ~ 5 for stars where they could compare results with and without measured EUV DEMs. In the case of LTT 1445A and GJ 486 we do not have direct flux measurements at EUV wavelengths, so this error is unavoidable and we cannot know how much the EUV flux is over-estimated in our analysis. However, we do note that by sampling the parameters that describe the DEM function, a lack of data increases the resulting uncertainty. This is most apparent in the case of LTT 1445A where we do not have as much temperature-coverage for the DEM function in the range of $6.0 < \log_{10}(T) < 6.5$. The resulting LTT 1445A spectrum is more likely to suffer from the over-prediction noted by Del Zanna et al. (2002); however the fitted DEM also has a greater uncertainty, and so the EUV flux error of the resulting spectrum encompasses a factor of 5 at the 1σ level in almost all EUV flux bins, and at the 2σ level in all EUV flux bins.

4.5. Optical and infrared

To fill in the optical and infrared end of the panchromatic spectra we used BT-SETTL (CIFIST) models that cover the optical to infrared part of the spectrum out to $20\mu\text{m}$ (Allard et al. 2003, 2007, 2011, 2012, 2013; Barber et al. 2006; Caffau et al. 2011) accessed from the Spanish Virtual Observatory database repos-

⁵ As outlined in the SAS threads: <https://www.cosmos.esa.int/web/xmm-newton/sas-threads>

⁶ See Brown et al. (2023) for a discussion on quiescent M dwarf coronal temperatures

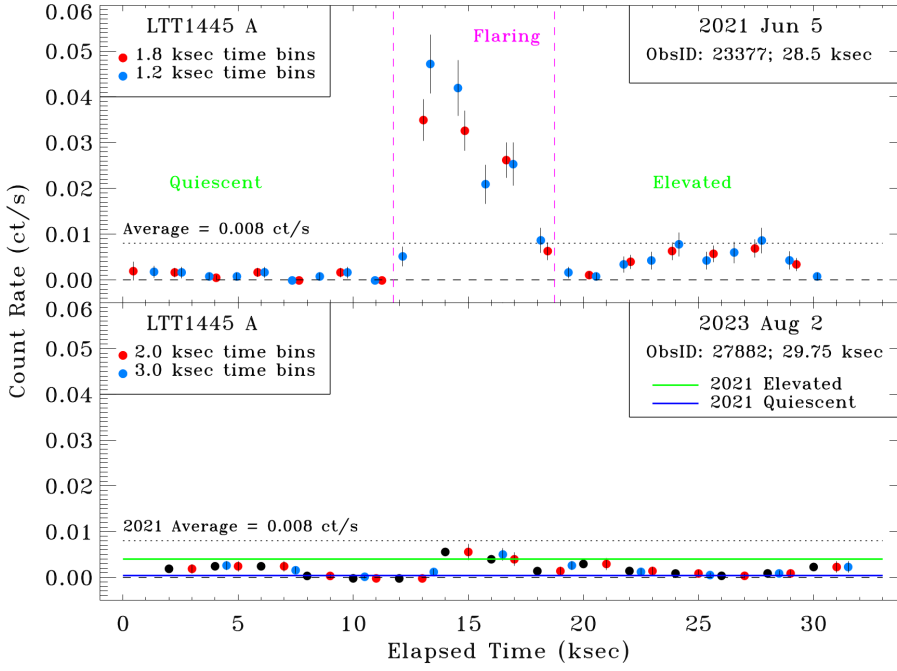


Fig. 9. X-ray observations of LTT 1445A using *Chandra* ACIS-S4. Observations from 2021 (top panel) were already reported in Brown et al. (2022). The 2021 observations distinctly show a flare. We use the observations from 2023 (Obs ID 27882, PI Howard) as representative of the typical X-ray state of LTT 1445A (bottom panel).

Table 5. X-ray source properties for LTT 1445A

	<i>Chandra</i> ACIS-S4		
	2021 Quiescent	2021 Flare	2023 All
ObsID (PI)	23377 (Brown)		27882 (Howard)
Exp. time (ks)	12.2	6.66	29.75
Source counts (ct)	4.9	177	50
Count rate (ct/ks)	0.4 ± 0.2	26.6 ± 2.0	1.68 ± 0.25
X-ray Flux (10^{-13} erg/cm ² /s)	0.066 ± 0.033	3.61 ± 0.27	0.51 ± 0.08
Characteristic Temperature (keV)	0.5 ^a	1.02 ± 0.10	0.55 ± 0.20
$\log_{10}(L_X)$ (erg/s)	$25.57^{+0.18}_{-0.30}$	27.31 ± 0.03	26.46 ± 0.04

Notes. Values from 2021 reproduced from Brown et al. (2022). Log fluxes calculated assuming stellar distance provided in Table 1.
^a We assume this temperature from the measurement from the elevated flux post-flare; it is in agreement with the 2023 observations.

Table 6. X-ray source properties for GJ 486

	<i>XMM-Newton</i> EPIC-pn		<i>Chandra</i> HRC-I
	Quiescent	Flare 1	All
Energy range (keV)	0.2–2.4		0.1–10
Wavelength range (Å)	5.2–62		1.2–124
Obs ID (PI)	0892010101 (Co-PI King)		26210/27799/27942 (Youngblood)
Exp. time (ks)	26.02	1.73	31.54
Source counts (ct)	109 ± 15	33.2 ± 6.4	55.8 ± 7.8
Count rate (ct/ks)	4.18 ± 0.57	19.2 ± 3.7	1.77 ± 0.25
X-ray Flux (10^{-14} erg/cm ² /s)	$0.80^{+0.68}_{-1.64}$	$4.35^{+0.61}_{-0.83}$	1.88 ± 0.27
Temperature 1 (keV)	$0.115^{+0.022}_{0.021}$		0.19 (assumed)
Temperature 2 (keV)	$0.783^{+0.097}_{0.099}$		n/a
$\log_{10}(L_X)$ (erg/s)	$25.797^{+0.035}_{-0.099}$	$26.531^{0.057}_{0.092}$	26.17 ± 0.07

Notes. The “Flare 1” spectrum also includes the underlying quiescent emission at that epoch. The spectrum for the second flare had insufficient signal to warrant fitting. Flux is the unabsorbed flux at Earth. Log luminosities calculated assuming stellar distance provided in Table 1.

itory⁷ (Bayo et al. 2008). The grid of stellar spectra were interpolated to the published values of effective temperature T_{eff} and surface gravity $\log(g)$ for LTT 1445A (Winters et al. 2019, 2022) and GJ 486 (Trifonov et al. 2021; Passegger et al. 2019).

Blue-ward of ~ 6000 Å model spectra of M dwarfs do not accurately reproduce measured stellar flux (e.g., Fontenla et al. 2016). To determine how reliably we can append a stellar model to the HST data, we compared the STIS/G430L observations

⁷ <http://svo2.cab.inta-csic.es/theory/main/>

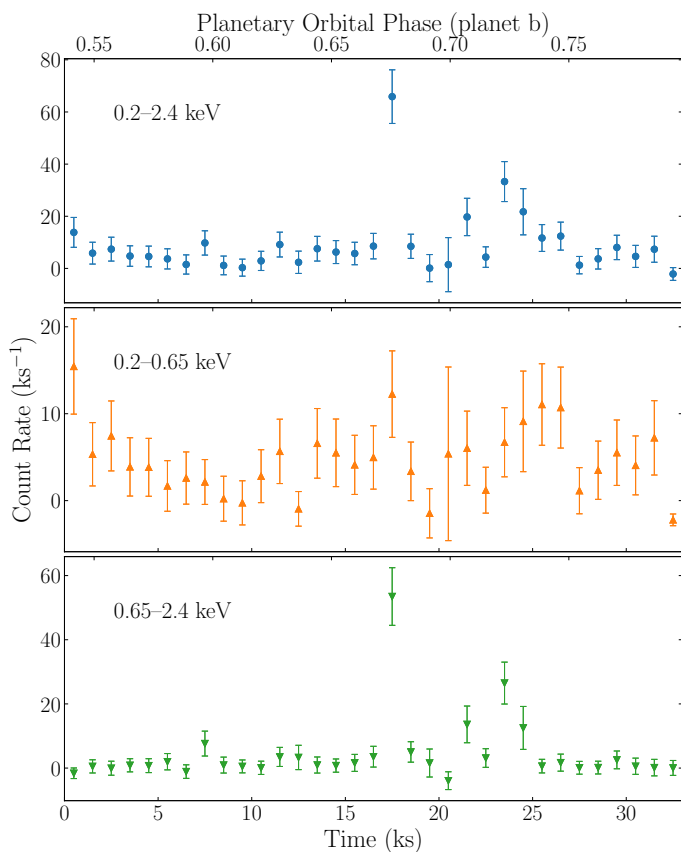


Fig. 10. *XMM-Newton* EPIC light curve of GJ 486 from the 2021 Dec 23 observation. The count rates are co-added across the three EPIC cameras (pn, MOS1 and MOS2). The three panels show the count rate in three bands: 0.2–2.4 keV (top), 0.2–0.65 keV (middle), and 0.65–2.4 keV (bottom).

with spectral data from *Gaia* DR3 BP/RP⁸ (*Gaia* Collaboration et al. 2023), as well as the interpolated stellar model. The STIS/G430L and *Gaia* data agreed where they overlap in wavelength. The interpolated BT-Settl (CIFIST) model broadly agreed with the *Gaia* spectra down to $\sim 5500\text{\AA}$ but at shorter wavelengths the model over-predicted the amount of flux measured by HST/STIS G430L and *Gaia* DR3 (Fig. 13).

We also compared interpolated stellar spectra from PHOENIX (Husser et al. 2013) and SPHINX (Iyer et al. 2023) models, which also over-predicted the stellar flux at short wavelengths. This over-prediction of flux by stellar models is one reason why having measurements from STIS/G430L out to 5700\AA is so valuable, especially for M dwarfs. We chose to use the BT-Settl (CIFIST) models because the PHOENIX models do not extend far enough into the infrared and the SPHINX models have less agreement with the *Gaia* and HST data. To complete our panchromatic spectra, we append BT-Settl (CIFIST) models interpolated to the parameters of LTT 1445A and GJ 486 to the red end of the HST spectra.

4.6. Putting it all together

For both LTT 1445A and GJ 486 we provide panchromatic spectra representing the quiescent state of each star. These spectra range from 1\AA – $20\mu\text{m}$ and are available on the *mstarpanspec*

high level science product (HLSP) page of the MAST archive⁹. As with previous works, the panchromatic spectra are available in four different versions:

- Variable resolution reflecting different instrument and model resolutions
- Constant resolution binned to 1\AA
- Variable resolution, adaptively binned to remove negative flux
- Constant resolution at 1\AA , adaptively binned to remove negative flux

Characteristic spectral properties for LTT 1445A and GJ 486 are provided in Table 7, and panchromatic spectra are shown in Figs. 14 and 15.

5. Flare analysis

Both LTT 1445A and GJ 486 exhibit flares in the UV and X-ray observations. These data are not simultaneous, nor do they cover the same wavelengths, so we cannot determine broadband flare characteristics (e.g., flare temperatures; Berger et al. 2023; Jackman et al. 2023). We also cannot compare the flare energies between the UV and X-ray flares. We therefore address the UV and X-ray flares separately.

5.1. Ultraviolet flares

Following the works of Loyd & France (2014) and Loyd et al. (2018) we used the *costools* package provided by STScI in order to flux-calibrate the time-series data. We detected one partial flare from LTT 1445A with the COS/G160M grating (Fig. 1). Unfortunately we did not catch the peak of this flare, only a partial decay at the beginning of an orbit. Without any constraints on the flare peak we cannot constrain the duration or energy of this flare, and we therefore do not provide any further analysis.

In the HST observations of GJ 486 we saw two flares, both with the COS/G130M grating (Fig. 2). For the first flare we have data before, during, and after the flare. The second flare is much larger and there is a gap in the data when the flare starts due to a change in FP-POS, however we did capture the flare peak. For neither flare do we observe a complete return to the pre-flare quiescent flux level. For both of GJ 486’s flares we employed the continuous flare model from Tovar Mendoza et al. (2022), which is an upgrade to the piece-wise analytic model for classical flares from Davenport et al. (2014). The Tovar Mendoza et al. (2022) flare model is a convolution of a Gaussian function with the sum of two exponential functions. The choice of a Gaussian function is physically motivated by the rapid rise in continuum emission, and the double exponential describes the rapid and then more gradual decay back to quiescence (Hawley & Pettersen 1991; Kowalski et al. 2013; Hawley et al. 2014; Davenport et al. 2014; Jackman et al. 2018, 2019).

Tovar Mendoza et al. (2022) provide an analytic flare model based on photometric optical data from the Kepler survey. This analytic model can be scaled by an amplitude, a characteristic timescale, and a central time to fit to new flares. We found that the analytic model fits the first GJ 486 flare reasonably well, but did not provide a good fit to the second, larger flare, which appears to have a longer rise timescale. It is possible that because the analytic model was derived using fits to optical flare data, it is not directly applicable to flares at broad UV wavelengths (Berger

⁸ <https://gaia-dpci.github.io/GaiaXPy-website/>
DOI v2.1.0: 10.5281/zenodo.8239995

⁹ <https://archive.stsci.edu/hlsp/mstarpanspec>

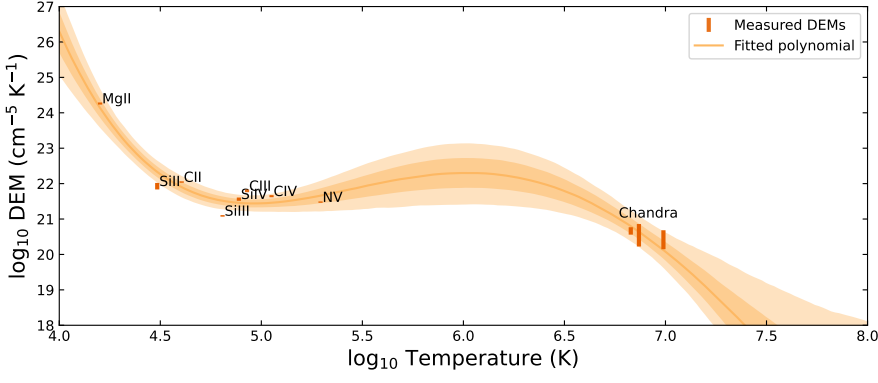


Fig. 11. Differential emission measures (DEM) with 1σ uncertainties derived from measured UV flux from HST/COS and X-ray flux from *Chandra* ACIS of LTT 1445A. We show the fifth-order Chebyshev polynomial best fit to the local DEMs along with shaded regions representing the 1σ and 2σ uncertainties for the fit.

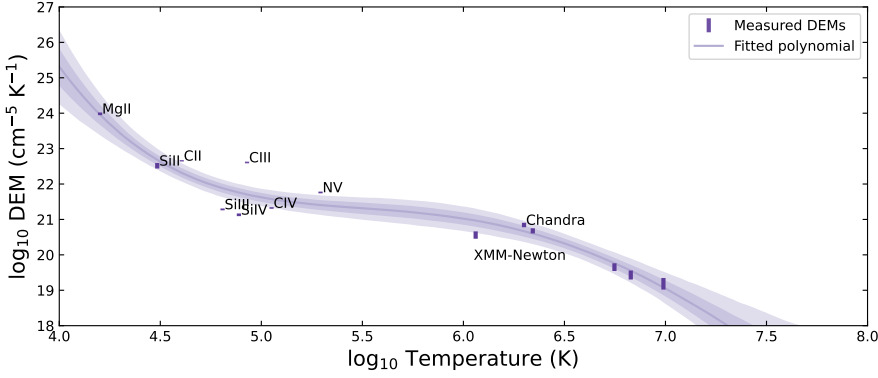


Fig. 12. Same as Fig. 11 but for GJ 486. All X-ray DEMs are derived from *XMM-Newton* observations, except for the single point from *Chandra* HRC-I.

Table 7. Derived spectrum values

	Wavelength	LTT 1445A		GJ 486
$\log_{10}(L_{\text{Bol}})$	1Å–20μm	31.49		31.66
$f(\text{XUV})$	1–912Å	-3.45		-4.55
$f(\text{FUV})$	912–1700Å	-4.33		-4.64
$f(\text{XUV}_{\text{age}})$	5–1700	-3.40		-4.30
$f(\text{NUV})$	1700–3200Å	-4.20		-4.41
FUV/NUV	—	0.75		0.58
Lyα/FUV	—	0.57		0.49
		LTT 1445Ab	LTT 1445Ac	GJ 486b
$F_{\text{XUV,p}}$ (erg/cm ² /s)	1–912Å	2.67×10^3	5.49×10^3	1.50×10^3

Notes. We compute $f(\text{band}) = \log_{10}(L_{\text{band}}/L_{\text{Bol}})$, where L_{Bol} is in units of erg s^{-1} . The value $F_{\text{XUV,p}}$ is the integrated XUV flux (1–912Å) received by each planet, assuming orbital distance a from Table 1. We provide the value $f(\text{XUV}_{\text{age}})$ because it is used to calculate stellar ages in Sect. 6.2 based on the XUV activity–age relationship from Engle (2024).

et al. 2023). Feinstein et al. (2022) also find that the analytic optical model did not match high-energy UV flares detected from the active star AU Mic. We therefore determined a new model fit to each flare following the methods in Tovar Mendoza et al. (2022), rather than using the analytic form derived from Kepler photometry.

$$\text{Flare}(t) = \frac{\sqrt{\pi}AC}{2} \left[\begin{array}{l} F_1 \left(\begin{array}{l} e^{-D_1 t_{\text{rel}} + (\frac{B}{C} + \frac{D_1 C}{2})^2} \\ \times \text{erfc}(\frac{B-t_{\text{rel}}}{C} + \frac{D_1 C}{2}) \end{array} \right) \\ + F_2 \left(\begin{array}{l} e^{-D_2 t_{\text{rel}} + (\frac{B}{C} + \frac{D_2 C}{2})^2} \\ \times \text{erfc}(\frac{B-t_{\text{rel}}}{C} + \frac{D_2 C}{2}) \end{array} \right) \end{array} \right], \quad (1)$$

where

- A is the flare amplitude;
- B is the central position of the Gaussian function;
- C is the Gaussian rise timescale;
- D_1 is the rapid decay phase timescale;

A full derivation of the flare model can be found in Tovar Mendoza et al. (2022), so here we only reproduce the final flare equation, after the convolution of the Gaussian and exponential functions has been applied:

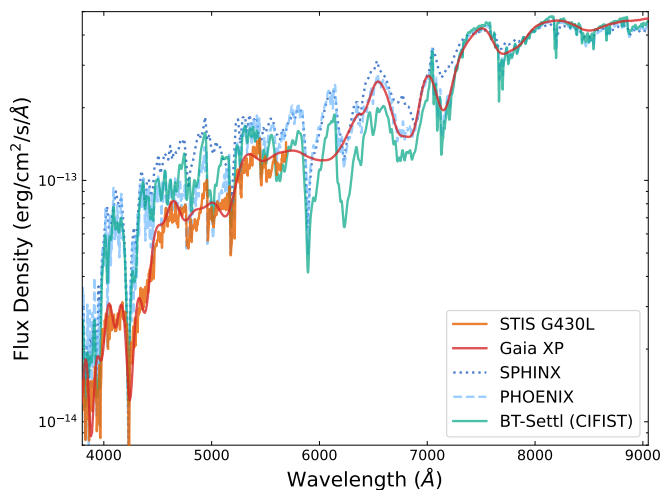


Fig. 13. Comparison of flux measured with HST/STIS and the G430L grating, *Gaia* DR3 spectra, and model spectra from SPHINX (Iyer et al. 2023), PHOENIX (Husser et al. 2013), and BT-Settl (Caffau et al. 2011) interpolated to the published parameters of LTT 1445A. No relative scaling was performed. The STIS/G430L and *Gaia* XP data agree where they overlap. We use the BT-Settl model in the panchromatic spectrum.

- D_2 is the slow decay phase timescale;
- F_2 is defined as $1 - F_1$, which describes the relative importance of the exponential decay terms D_1 and D_2 ; and
- *erfc* is the complementary error function from `scipy.special`.

The flare model is a function of relative time t_{rel} , which is the unitless value defined as

$$t_{\text{rel}} = \frac{t - t_{\text{cen}}}{t_{1/2}}, \quad (2)$$

where t is time, t_{cen} is a central time that is close to the time of the flare peak, though not exactly at the flare peak due to the convolution, and $t_{1/2}$ is the characteristic timescale (Kowalski et al. 2013). This scaling to a relative time is useful when fitting multiple flares because the priors for the flare function variables only need to be defined once, as opposed to being tailored to each flare.

Again following Tovar Mendoza et al. (2022), we determined the best-fit flare model for each flare by performing the following steps:

1. Subtract off the median out-of-flare flux such that the baseline is at 0.
2. Fit the flare using the analytic flare model from Tovar Mendoza et al. (2022) to determine initial flare scaling parameters: amplitude, central time, and characteristic timescale.
3. Scale the flare by the initial flare scaling parameters and fit for the flare model variables A , B , C , D_1 , D_2 , and F_1 .
4. Fix the best fit flare model variables and then again fit for the flare scaling parameters to get the best-fit flare model.

In both flare cases we did not capture enough data post-flare to see the flux return to the nominal pre-flare flux level; we therefore only used the pre-flare flux level to compute the median out-of-flare flux. We used the `emcee` package built into the `lmfit` optimizing package to explore the parameter space (Foreman-Mackey et al. 2013; Newville et al. 2016). We ran `emcee` for

50,000 steps with a 5,000 step burn in and determined convergence by checking the integrated auto-correlation time. We report our best-fit values in Table 8.

To compare the two flares we detected from GJ 486 with those from other works (e.g., Loyd et al. 2018), we used the best-fit flare model and the median out-of-flare flux value to compute the absolute energy E (the integrated flux during the flare minus the quiescent flux) and equivalent duration δ (the flare energy normalized by the quiescent energy) for each flare, using the standard equations for these values (Loyd et al. 2018). Because we did not observe the return to the quiescent flux level after either flare, in both cases we extended the best-fit model past the end of the observations in order to compute the absolute energies and equivalent widths. We also computed flare parameters from the best-fit flare models, such as time of the flare peak, flare amplitude, and flare fwhm (Table 8).

We additionally inspected how the two flares affect individual transition lines in the FUV observed with the COS/G130M grating. We reiterate that, at the beginning of the analysis, we removed time-series data containing the flares from the rest of the observations used to make the panchromatic spectrum. We used the removed flare data to create FUV spectra and fit the line profiles of observed transition region lines using the same methods as described in Sect. 4.1.

We compared the flux density of each line between the quiescent state and each flare state (Fig. 17). The flare data are shown in purple, with purple lines representing the best-fit Voigt line profiles convolved with the COS LSF. These are compared to the best-fit line profiles from the quiescent data (black lines). The transition region lines are ordered from lower to higher formation temperatures. It is not surprising that the more energetic Flare 2 shows a larger increase in individual transition region lines than Flare 1. Note that observations for Flare 2 used FP-POS 4, which does not cover the Si III line. The greatest increases in line flux are for lines forming at intermediate temperatures of $4.5 > \log_{10}(T) > 5.0$: C II, Si III, and C III (France et al. 2016; Loyd et al. 2018). In Flare 2 we also see emission from the coronal FUV line Fe XXI at 1354 Å.

5.2. X-ray flares

LTT 1445A flared during the 2021 *Chandra* observations and was analyzed in detail in Brown et al. (2022). We reproduce the flare time series in Fig. 9, along with the quiescent time series taken in 2023 and used in the panchromatic spectrum in this work. The flare flux is about 55× greater than the average quiescent level just prior to the flare, and about 7× greater than the quiescent level observed two years later in 2023. The characteristic single-temperature fits to these spectra show significantly hotter plasma present during the flare than in quiescence (see Table 5).

The LTT 1445A datasets obtained in ACIS VFaint mode (Fig. 9) were tested for source variability using the CIAO tool `glvary`¹⁰. This tool searches for variability using the Gregory-Loredo algorithm (Gregory & Loredo 1992), which tests for non-random grouping of the event times across multiple time bins. The `glvary` tool is regularly used to test for variability in the major *Chandra* source catalogs and provides a variability index (VARINDEX) which ranges from 0 to 10, with values of 5 or above indicating a variable source. The 2021 observation with its large flare has a VARINDEX of 10. The 2023 observation, while less dramatic, is also definitely variable with a VARINDEX of 7.

¹⁰ `glvary` CIAO thread: xc.cfa.harvard.edu/ciao/threads/variable/

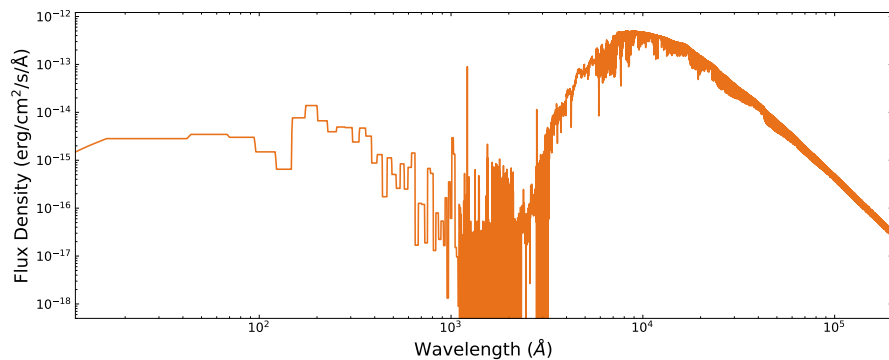


Fig. 14. Panchromatic spectrum of LTT 1445A from 1 \AA – $20\text{ }\mu\text{m}$ constructed from empirical data in the X-ray, UV, and optical (HST/COS and STIS, *Chandra*), estimates of the EUV (using the DEM method), a $\text{Ly}\alpha$ line reconstruction, and models of the optical and infrared (BT-Settl).

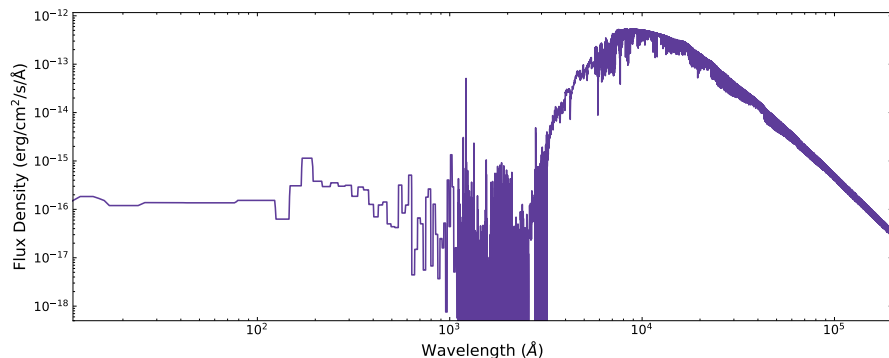


Fig. 15. Panchromatic spectrum of GJ 486 from 1 \AA – $20\text{ }\mu\text{m}$ constructed from empirical data in the X-ray, UV, and optical (HST/COS and STIS, *Chandra*, *XMM-Newton*), estimates of the EUV (using the DEM method), a $\text{Ly}\alpha$ reconstruction, and models of the optical and infrared (BT-Settl).

Table 8. GJ 486 flare properties

	Unit	Flare 1	Flare 2
Wavelength range	\AA	1065–1367	1065–1367
Flare start–end ^a	s	1730–2161	1300–2690
Flare duration ^a	s	431	1390
Median quiescent flux	$\text{erg cm}^{-2} \text{ s}^{-1}$	9.02×10^{-15}	8.89×10^{-15}
Flare model parameters			
t_{cen}	s	1809.60 ± 0.80	1438.22 ± 0.89
$t_{1/2}$	s	36.2 ± 1.8	89.6 ± 1.7
A	—	1.28 ± 0.19	1.50 ± 0.10
B	—	-0.182 ± 0.041	-0.164 ± 0.020
C	—	0.364 ± 0.061	0.536 ± 0.026
D_1	—	0.015 ± 0.017	0.226 ± 0.014
D_2	—	1.16 ± 0.13	1.8 ± 0.16
F_1	—	0.0327 ± 0.0058	0.0988 ± 0.0067
Derived flare properties			
Time of peak flare ^a	s	1814	1457
Flare amplitude	$\text{erg cm}^{-2} \text{ s}^{-1}$	2.34×10^{-13}	8.36×10^{-13}
FWHM	s	47	123
Absolute energy ($E_{\text{COS/G130M}}$)	erg	$3.065 \pm 0.068 \times 10^{29}$	$1.368 \pm 0.012 \times 10^{30}$
Equivalent duration (δ)	s	4357 ± 96	19724 ± 169

Notes. A description of the flare model parameters can be found in Sect. 5.1. Derived flare properties are computed from the best-fit flare models.
^a Flare times are relative to the observation start time. We do not observe the start of Flare 2, so time values are approximate.

The variability seen in the 2023 dataset seems to be typical for LTT 1445A.

For GJ 486 we observed flares with the *XMM-Newton* EPIC-pn camera, as shown in Fig. 10. The biggest flare occurred about halfway through the observation, and is clearly visible in the harder energies (bottom panel), with only a smaller, nonsignificant rise in the soft band (middle panel). Our spectral fits in Sect. 4.3 indicate a $5.5\times$ increase in the overall flux during the flare, with the bulk of that rise coming through an increase in the

higher of the two temperature components. This “hardening” of the X-ray emission is typical of flares at these wavelengths (e.g., Reale et al. 2001; Pye et al. 2015).

Two small peaks in the following ~ 7 ks are also possibly associated with flaring, with both rises only seen in the hard band and not the soft. The first is not statistically above the basal level, and was not excluded from the quiescent epoch in our spectral fits in Sect. 4.3. The peak of the second does show a clear significant rise above the quiescent level. The signal was too low

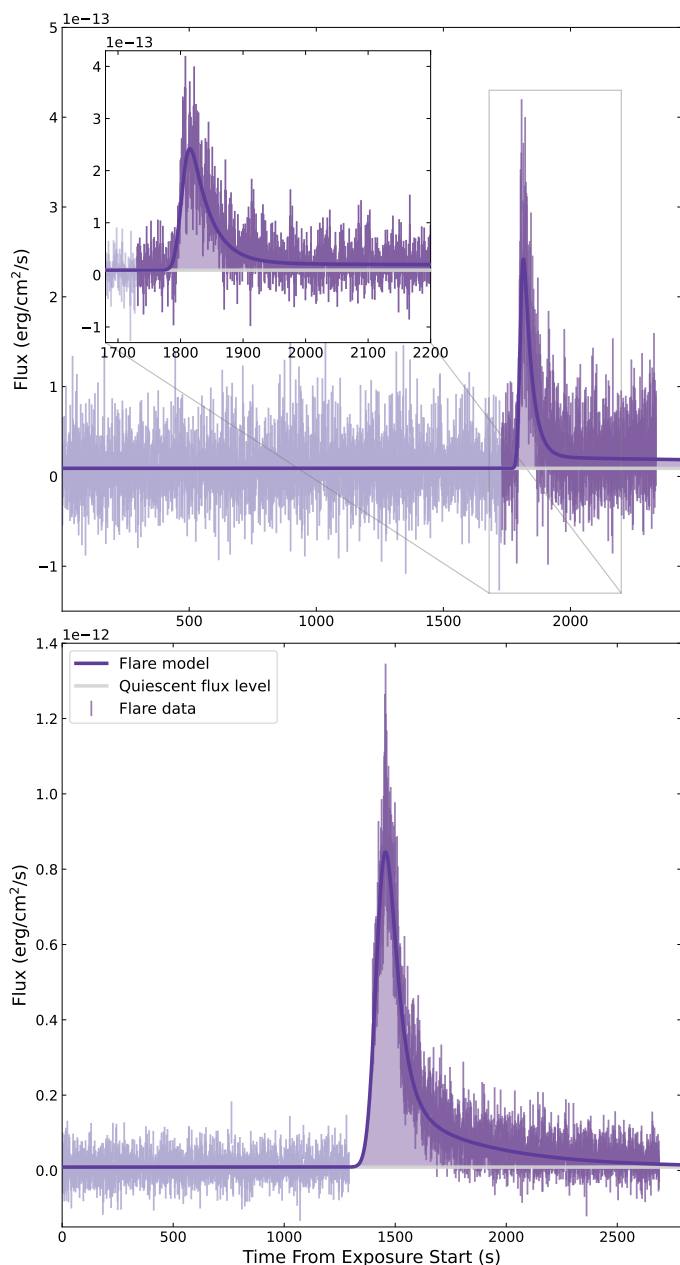


Fig. 16. We detected two flares in the time series of the COS/G130M data for GJ 486. Dark purple points highlight the data that we consider to be “in flare,” as opposed to the lighter purple “quiescent” data. Dark purple lines are the best-fit flare models (Eqn. 1, Table 8), created from a continuous flare model based on the work of Tovar Mendoza et al. (2022). The first flare (Flare 1; *top*) has an absolute energy of $10^{29.5}$ erg and an equivalent duration of 4357 ± 96 s, while the second flare (Flare 2; *bottom*) is larger, with an absolute energy of $10^{30.1}$ erg and an equivalent duration of 19724 ± 169 s.

to warrant fitting a separate spectrum, but this epoch was not included the quiescent spectrum.

We attempted to search for evidence of the flaring in the simultaneous near-UV data taken with the OM. Looking at the raw image mode count rates shows evidence of a possible rise shortly after the midpoint of the observation. However, the data also show major problems. While much of the background in a single exposure shows ~ 10 counts per pixel, there are many with $> 10,000$ counts spread all across the image. While suggestive of guiding issues and/or the source being too bright, there is

still a source visible in the correct position on the image, and the hallmarks of typical OM saturated sources are not present. The problems seen in the OM data lead the later parts of the standard reduction chains to fail. We do not consider this data further.

5.3. Flare frequency

Based on the observed flares and Poisson counting statistics we make rough approximates of flare frequencies. Optical activity indicators suggest that both LTT 1445A and GJ 486 can be considered inactive stars. From two sectors of TESS data on GJ 486, a visual inspection did not reveal any flares. The TESS photometric light curve for LTT 1445A is contaminated by an active binary companion $7''$ away; there are many flares in the LTT 1445A TESS light curve, but their origin is likely from LTT 1445B and C, and the three components cannot be disentangled to determine the flare origins.

From the two GJ 486 flares observed in the FUV with the COS/G130M grating (observations that lasted a total of 7610 s), we derive a flare frequency 23 ± 5 flares/day with absolute energy $E \geq 10^{29.5}$ erg and equivalent duration $\delta \geq 4,300$ s. We compare this estimate directly to work by Loyd et al. (2018), who used observations with the same COS/G130M grating to perform a statistical analysis of flares in sample of 10 active and inactive M dwarfs. We find that the derived flare frequency for GJ 486 in this work is similar to what we expect for typically active M dwarfs when comparing absolute energies (Loyd et al. 2018). However, Loyd et al. (2018) demonstrated that flare frequencies for inactive and active M dwarfs are statistically indistinguishable when comparing flares in relative units, such as equivalent duration. When comparing the derived flare frequency for GJ 486 to the Loyd et al. (2018) sample we find that the supposedly inactive GJ 486 flares at a rate of more than $10\times$ that of the stars in the Loyd et al. (2018) sample. For LTT 1445A we detected a flare, but because we cannot determine its energy or duration, we cannot derive a UV flare rate.

The relationship between flare energy in the UV and X-ray is not well established, with only limited information available regarding the relative strengths of a single flare event across the electromagnetic spectrum (MacGregor et al. 2021). Simultaneous observations in X-ray and FUV did observe flares on Proxima Centauri and found a coherent increase in the derived DEM corresponding to the X-ray and FUV regimes (Fuhrmeister et al. 2022). While we observed X-ray flares for both LTT 1445A and GJ 486, these are not the counterparts to the UV flares, which were observed at different times. The X-ray time series data are not flux-calibrated, meaning that we cannot derive X-ray flare frequency rates.

6. Discussion

6.1. Planetary atmospheres

A driving motivation for capturing the high-energy flux from exoplanet-hosting M dwarfs and producing self-consistent panchromatic spectra is to gain a holistic understanding of their terrestrial planets’ atmospheres. High energy flux from M dwarfs influence both photochemistry and atmospheric escape from the upper atmospheres of orbiting planets (Catling & Kasting 2017; Kubyshkina 2024). The photoevaporation theory of atmospheric evolution posits that the terrestrial exoplanets we observe today may have started off with primordial hydrogen-rich atmospheres that were subsequently lost due to hydrodynamic escape (Owen & Wu 2013; Lopez & Fortney 2013; Luger et al. 2015; Owen

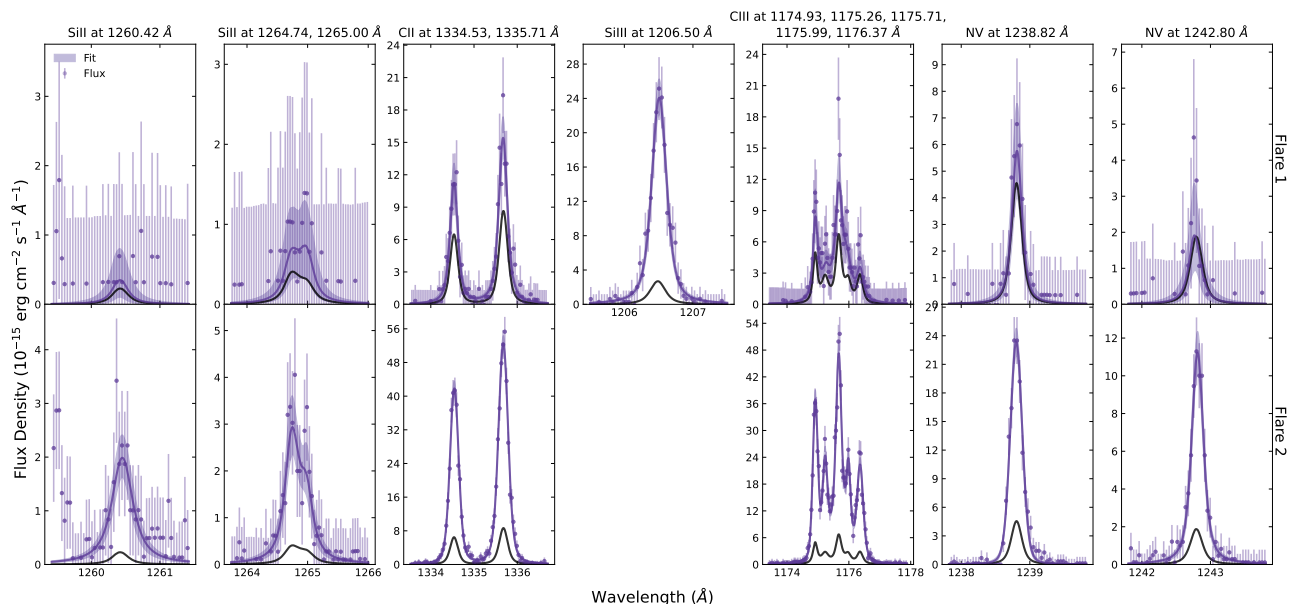


Fig. 17. Transition region lines detected with COS/G130M for GJ 486 during the two observed flares. The purple line profiles and fits are constructed from data taken during the “in flare” phase of each flare. The black line profiles are the quiescent states; they are the same quiescent profiles in the top and bottom rows, but note the change in y-axes. Flare 2 was observed using FP-POS 4, which misses the Si III line at 1206.5 Å.

et al. 2020). Hydrodynamic escape is driven by the absorption of stellar high energy radiation in the upper atmospheres of planets. As hydrogen is driven away, it can drag heavier material along with it, leading to loss of atomic and molecular species such as O, H₂O, and CO₂ (Zahnle & Kasting 1986; Pepin 1991; Odert et al. 2018; Lammer et al. 2018). Photodissociation of H₂O can continuously fuel hydrodynamic escape, and in the extreme lead to complete dessication of the planet (Luger & Barnes 2015), as perhaps is the case for Venus (e.g., Gillmann et al. 2009).

Early hydrodynamic escape is rapid, and can last from a few thousand years to a few Myr after formation, depending on a planet’s initial water content and atmospheric composition, and the stellar high energy flux. Hydrodynamic escape can result in the complete loss of atmospheric atomic hydrogen, as well as losses of a few to a few thousands of bars of heavier species, again depending on the initial conditions. For example, in a study focused on the terrestrial exoplanet TRAPPIST-1c orbiting a late-type M dwarf, Teixeira et al. (2024) impose initial water contents of 0.01 to 100 Earth oceans on TRAPPIST-1c, and find that hydrodynamic escape can last for 1000 years to 10 Myr resulting in a loss of CO₂ ranging from 0.1 to 1000 bars.

The measured radii and masses of the terrestrial planets LTT 1445Ab, LTT 1445Ac, and GJ 486b result in high bulk densities that are inconsistent with H/He-rich atmospheres (Trifonov et al. 2021; Winters et al. 2022), and, based on hydrodynamic escape models, we do not expect these worlds to currently retain primordial H/He-dominated atmospheres accreted from the protoplanetary nebula (Kubyskhina & Vidotto 2021). It is possible, however, that these worlds have secondary atmospheres consisting of heavier molecular material than hydrogen that is not so easily lost. Secondary atmospheres can arise from material that was sequestered in the mantle during formation and outgassed later on timescales of a few Gyr (e.g., Marty & Dauphas 2003), or else delivered by comets or asteroids (Raymond et al. 2007; Ciesla et al. 2015; O’Brien et al. 2018). Secondary atmospheres can still be sculpted and removed by stellar wind, which is particularly relevant for terrestrial exoplanets on short orbital periods around M dwarf stars (e.g., Garraffo et al. 2017). It is also

possible that LTT 1445Ab, LTT 1445Ac, and GJ 486b are airless rocks (e.g., Kreidberg et al. 2019; Crossfield et al. 2022; Zieba et al. 2023; Zhang et al. 2024).

To connect the measured X-ray and EUV radiation from the M dwarfs LTT 1445A and GJ 486 to the atmospheric mass loss of their terrestrial exoplanets, we employ a toy model following the steps of (Teixeira et al. 2024). We skip the rapid hydrodynamic escape phase since the mass loss is heavily dependent on initial water content, for which we do not have accurate estimates, and it is clear from radius-mass measurements that LTT 1445Ab, LTT 1445Ac, and GJ 486b do not have hydrogen-dominated atmospheres. We instead focus on whether or not pure CO₂ secondary atmospheres on these worlds can survive to the present day in the presence of stellar wind, though atmospheres can also be sculpted and stripped over long timescales via thermal processes such as Jeans escape (Van Looveren et al. 2024). Our toy model does not include rates of mantle outgassing or the possibility of magnetic fields on the planets, which can shield atmospheres from stellar ions.

We use the X-ray luminosity–age relationship developed by Engle (2024) for M2.5–6.5 dwarfs to get an estimate of the X-ray luminosity over time for the two targets, up until their current estimated ages (details on stellar ages to follow in Sect. 6.2). We then calculate the stellar mass loss rates following Teixeira et al. (2024), who derive their stellar mass-loss rate relationship from Wood et al. (2021):

$$\dot{M}_s = \frac{\mathcal{A}}{10^{3.42}} F_{X,\text{surf}}^{0.77}, \quad (3)$$

where \mathcal{A} is the stellar surface area in solar units, and $F_{X,\text{surf}}$ is the X-ray surface flux of the star. The result is the stellar mass loss rate in units of solar mass loss rate, which we take as 1.26×10^{12} g/s.

From the stellar mass loss rate we calculate the planetary atmospheric mass loss rate due to stellar wind stripping as

$$\dot{M}_{\text{atm}} = 0.025 \left(\frac{R_p}{a} \right)^2 \dot{M}_s, \quad (4)$$

where R_p is the planetary radius and a is the planetary semi-major axis (Dong et al. 2018; Teixeira et al. 2024). The factor of 0.025 is borrowed from the TRAPPIST-1 system because we do not have MHD models of LTT 1445A or GJ 486; however they are also M dwarfs and their planetary orbital distances are similar to those of the TRAPPIST-1 planets (Agol et al. 2021).

When executing the toy models we assume pure CO_2 atmospheres for LTT 1445Ab, LTT 1445Ac, and GJ 486b, since CO_2 is a common atmospheric molecule with advantages for atmospheric retention: it has a high mean molecular weight and a rapid cooling timescale that makes it resilient to thermal escape (Gordiets & Kulikov 1985; Johnstone et al. 2021; Van Looveren et al. 2024). For each planet we start with a pure CO_2 atmosphere equal to 5–50% of Earth’s total estimated CO_2 budget of 10^{22} mol (Sleep & Zahnle 2001; Foley & Smye 2018). Though we do not take into account outgassing rates, Teixeira et al. (2024) find that most of the outgassing takes place in the first Gyr. For each time step, we compute the planetary atmospheric mass loss rate from the stellar mass loss rate, and subtract the result from the remaining CO_2 in the atmosphere.

We present the results of our toy model in Fig. 18. Whether or not the planets LTT 1445Ab, LTT 1445Ac, and GJ 486b, can retain CO_2 -rich atmospheres is dependent on their initial atmospheric CO_2 content, their orbital distances, and the age of their host stars. So long as LTT 1445Ab has an initial CO_2 budget of at least 10% that of Earth’s, it should be able to maintain a CO_2 atmosphere of at least 1 bar of surface pressure. LTT 1445Ac, which orbits closer to the host star, needs at least 15% of Earth’s CO_2 budget to maintain an atmosphere of almost 1 bar of surface pressure. Finally, GJ 486b orbits the closest to its host star, making its atmosphere the most susceptible to loss; GJ 486b needs an initial CO_2 content of at least 50% of Earth’s current CO_2 content to maintain a CO_2 -rich atmosphere of at least 1 bar of surface pressure.

Without knowing the initial compositions of LTT 1445Ab, LTT 1445Ac, and GJ 486b or the activity history of their host stars, we cannot know *a priori* whether or not they have atmospheres today. Determining whether or not these planets have atmospheres can place upper limits on their initial water contents (e.g. Kreidberg et al. 2019). One scaling relation called the “cosmic shoreline” compares the (estimated) cumulative XUV radiation received by a planet and its escape velocity under assumptions of energy-limited escape (Zahnle & Catling 2017). All three planets considered in this work lie close to the $I_{\text{XUV}} \propto v_{\text{esc}}^4$ relationship, implying that all three planets have undergone hydrogen-stripping but are not necessarily bare rocks. Observational programs looking at LTT 1445Ab and GJ 486b in secondary eclipse with JWST/MIRI LRS spectroscopy (GO Program 1743, PI Mansfield; and 2807 PI Berta-Thompson) and in transmission with JWST/NIRSpec BOTS (GO Program 2512, PI Batalha) may soon provide the answer for these two worlds.

6.2. Stellar ages

It is notoriously difficult to determine the ages of M dwarfs. They spend hundreds of Gyr on the main sequence (Choi et al. 2016), and once they are stably fusing hydrogen in their cores, their measurable properties like luminosity, effective temperature, and radius remain constant on cosmological timescales; in

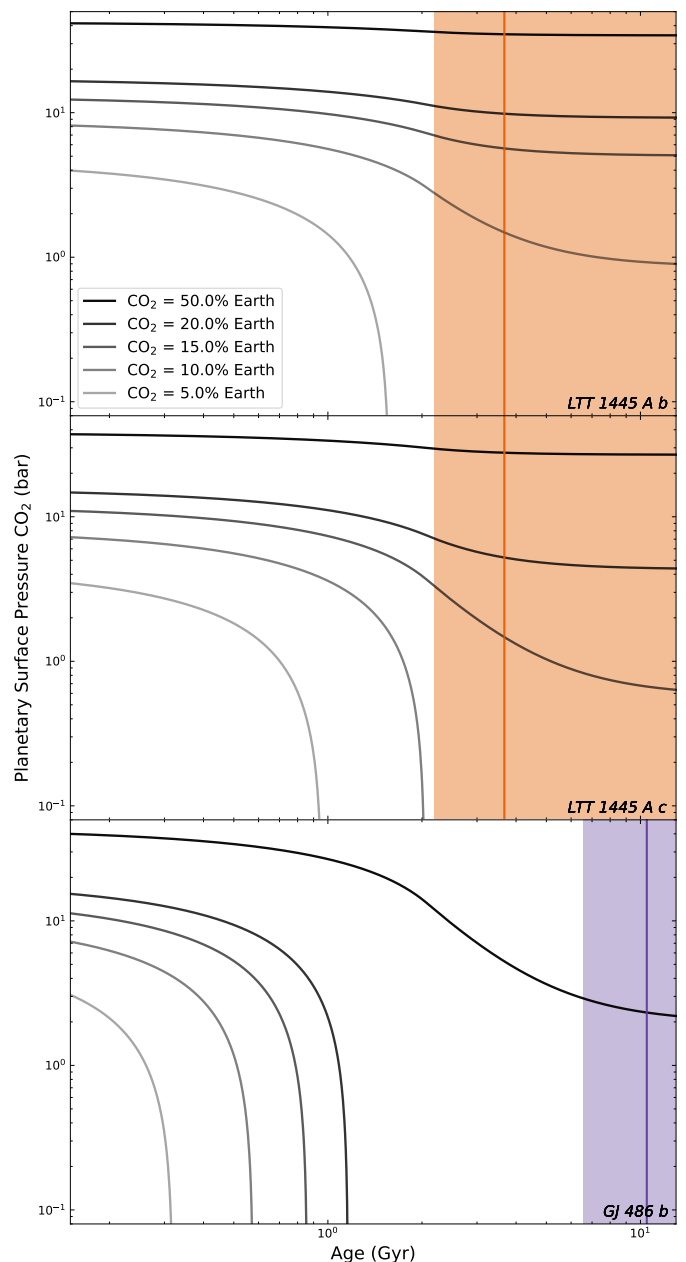


Fig. 18. Results of the toy model describing CO_2 mass loss from each terrestrial planet, assuming initial atmospheres of pure CO_2 5–50% that of Earth’s total estimated CO_2 content of 10^{22} mol (Sect. 6.1). The vertical orange and purple lines, along with the shaded regions, are the estimated stellar ages with uncertainties (discussed in Sect. 6.2). Whether or not each planet maintains a CO_2 atmosphere with surface pressure of ≈ 1 bar depends on the initial CO_2 content, the planetary orbital period, and the stellar age and activity history. The model does not take into account CO_2 outgassing rates—we assume all of the CO_2 outgasses at the start of the model time steps—or magnetic fields, which may be able to shield secondary atmospheres from loss.

other words, longer than the age of the universe. This means that stellar evolutionary models are poor predictors of M dwarf age, even with well-constrained stellar properties in the *Gaia* era (Gaia Collaboration et al. 2016, 2023; Eastman et al. 2023).

One promising avenue is to apply the age–rotation or age–activity relationships that exist for main sequence stars, and set constraints specifically for M dwarfs (Wright & Drake 2016; Wright et al. 2018). The fact that older main sequence stars have

longer rotation periods and decreased activity relative to younger main sequence stars is well-documented (e.g., [Schatzman 1962](#); [Skumanich 1972](#); [Barnes 2003](#); [Newton et al. 2016](#); [Pineda et al. 2021](#)). Using a series of dating methods to pinpoint the ages of a precious sample of M dwarfs, [Engle & Guinan \(2023\)](#) establish age–rotation relationships for early- to mid-M dwarfs, which are then expanded to age–activity relationships ([Engle 2024](#)). Here we apply some of these relationships to LTT 1445A and GJ 486.

Both LTT 1445A and GJ 486 have long rotation periods: 85 ± 22 and 130.1 ± 1.6 days, respectively ([Trifonov et al. 2021](#); [Winters et al. 2022](#)); and low activity: only weak measurements of H α and Ca II H & K ([Astudillo-Defru et al. 2017](#); [Hojjatpanah et al. 2019](#); [Winters et al. 2019](#)). These long rotation periods and weak activity indicators broadly put LTT 1445A and GJ 486 in the category of “old, inactive” M dwarfs, but here we attempt to derive more quantitative ages. Using the age–rotation relationships for M2.5–6.5 dwarfs with rotation period greater than 24 days, we estimate that the ages of LTT 1445A and GJ 486 are $5 \pm \text{Univ}$ and 7.8 ± 4.8 Gyr, respectively [Engle & Guinan \(2023\)](#), where we use the limit of “Univ” to mean that the uncertainties extend to the age of the universe. We also note that additional work on GJ 486 finds a significantly shorter stellar rotation period of 49.9 ± 5.5 days ([Caballero et al. 2022](#)), which translates to a stellar age of $3.7^{+5.1}_{-1.5}$ Gyr ([Engle & Guinan 2023](#)).

The unconstrained age of LTT 1445A is due to the difficulty in measuring its rotation period; the value of $P_{\text{rot}} = 85 \pm 22$ days is derived from the mass–rotation period relation for inactive M dwarfs ([Newton et al. 2017](#)). LTT 1445A is the primary member of a hierarchical stellar triple, with a binary pair roughly 7'' away. The binary stars are more active and have rapid rotation periods, making it difficult to distinguish the much longer rotation period of LTT 1445A ([Winters et al. 2022](#)). Based on an analysis of galactic kinematics and flare rates of a volume complete sample of mid-to-late M dwarfs, ([Medina et al. 2022](#)) determine broad age bins based on stellar rotation period: mid-to-late M dwarfs with $10 < P_{\text{rot}} < 90$ days are 5.6 ± 2.7 Gyr, and those with $P_{\text{rot}} > 90$ days are 12.9 ± 3.5 Gyr. These age-bin estimates agree with those found using the age–rotation relation from [Engle & Guinan \(2023\)](#).

We are better able to constrain the ages of LTT 1445A and GJ 486 using their high-energy spectra and age–activity relationships ([Engle 2024](#)). We opt to use the $\log(L_{\text{X-UV}}(5-1700\text{\AA})/L_{\text{bol}})$ activity–age relation because this is the best defined in terms of wavelength range. We integrate the panchromatic spectra from 5–1700 Å and find that LTT 1445A has an age of $3.7^{+1.5}_{-1.5}$ Gyr and GJ 486 has an age of $10.5^{+3.9}_{-3.9}$ Gyr. The upper and lower bounds of the stellar age are conservative: we take the integrated X-UV (5–1700Å) flux plus and minus 1σ errors on the panchromatic spectrum and compare these against the 1σ errors in the activity–age relationship from [Engle \(2024\)](#). We take the outermost ages that take into account the uncertainty in the integrated spectrum and the activity–age relation. We place lower limits on the ages of LTT 1445A and GJ 486 at 2.2 and 6.6 Gyr, respectively.

Conservatively, we cannot put an upper bound on the age of LTT 1445A and GJ 486; however the 1σ lower age bounds are still useful. For example, based on their flare-rate analysis as a function stellar rotation period, [Medina et al. \(2022\)](#) determine a transition age for mid-to-late M dwarfs from a saturated to unsaturated flaring state at 2.4 ± 0.3 Gyr, though we note that this result is based on optical flares in the TESS data. If this transition age is true for UV flares, then GJ 486 is in a state of decreased activity and relatively low flaring, while LTT 1445A may be in

the process of transitioning between the saturated and decreasing activity states. The UV flare rate we deduce for GJ 486 is significantly higher than what we expect for an inactive star, suggesting that high-energy flare rates may remain high as optical flare rates decrease.

6.3. Evidence of prolonged elevated activity

We do not have access to long-term high-cadence monitoring of a large sample of inactive M dwarfs at high-energy wavelengths. Rather, what we present here are high-cadence observations in spurts from HST. Based on these noncontiguous observations, we posit that supposedly “inactive” M dwarfs like LTT 1445A and GJ 486 not only produce more high-energy flares per day than in the optical, but also that those flares produce prolonged periods of heightened flux output, perhaps lasting as long as several days, and may be the result of observing during a high-activity period. Here we present evidence for this conjecture.

We look first at GJ 486 because for this star we observe two flares and are able to model them and derive their absolute energies and equivalent durations. It is well-documented that stars that are considered inactive at optical wavelengths still flare in the FUV ([Lloyd et al. 2018](#); [Froning et al. 2019](#); [Lloyd et al. 2020](#); [Diamond-Lowe et al. 2021](#); [Jackman et al. 2024](#)). The star GJ 674 is considered inactive with a rotation period of 30 days, no H α in emission, and an approximate age of 0.1 to a few Gyr ([Bonfils et al. 2007](#); [Newton et al. 2018](#)), and yet multiple flares, the largest having an absolute energy of $E = 10^{30.75}$ erg and an equivalent duration of $> 30,000$ s, were observed up by HST COS/G130M ([Froning et al. 2019](#)). By comparison, GJ 486 has an even longer rotation period of 130 days and a lower age limit of 6.6 Gyr, and two flares with absolute energies $E = 10^{29.5}$ and $E = 10^{30.1}$ erg and equivalent durations of 4357 ± 96 and 19724 ± 169 s were observed with the same grating within three hours. Old and quiet M dwarfs like GJ 486 can still produce high energy flares, but what is surprising is that we derive a flare frequency roughly 10 \times that of the broader M dwarf population ([Lloyd et al. 2018](#)), with the caveat that we are very much in the regime of small sample statistics based on the limited time-sampling of our observations. We find it more plausible that we caught GJ 486 in a period of heightened flare activity than this being the true flare frequency for this star.

We additionally posit that this period of heightened activity in GJ 486 lasts at least a week. We observed the two flares from GJ 486 in the same HST visit, only three hours apart ([Fig. 2](#)), perhaps suggesting that both flare events originate from the same activated region of the stellar surface. We showed in [Sect. 4.2](#) and [Fig. 8](#) that even after removing the flare data from the COS/G130M observations, the UV-UV line correlations with Ly α suggest that lines measured from the “quiescent” time series were in fact excited. The next set of UV observations of GJ 486 taken six days later with COS/G160M and COS/G230L, also appear systematically higher than what we estimate for the Ly α flux using the reconstruction method ([Youngblood et al. 2016](#)). The STIS/G140M observations that provide the data for the Ly α reconstruction were taken almost exactly one year apart—three months before the COS/G130M observations were we observe the flares and eight months after the COS/G160M and COS/G130M observations—yet they agree incredibly well. Our final line of evidence for prolonged activity comes from the LTT 1445A data, where we observed the tail end of a flare with COS/G160M. We do not know how big this flare was, but two days later we observed LTT 1445A with STIS/G140M, and this observation gives 1.5 \times higher flux than STIS/G140M observa-

tions taken six weeks before (Fig. 1). It is of course also possible that these older M dwarfs might exhibit sporadic rather than periodic activity. Indeed, previous searches did not find strong evidence for persistent flare periodicity in TESS data, though short-term periodic cycles may exist (Howard & Law 2021).

If there are indeed times of heightened stellar activity, whether periodic or not, in older quiet M stars, this affects our ability to determine their ages based on age–activity relations. X-ray and UV measurements of stars generally come from a handful of observations. Wherever a star happens to be in its activity cycle when we observe it will affect the resulting estimated age when using age–activity relations. A good example of this are the three X-ray states—“quiescent,” “flare,” and “elevated”—of LTT 1445A reported by Brown et al. (2022), and the resulting placement of the star on the X-ray–age relationship based on each state (Fig. 4 of that paper). Poor time-sampling of high-energy stellar observations are likely contributing to the scatter in the activity–age relationships at both X-ray and UV wavelengths.

Ultimately, we have exhausted the detective work we can do with our noncontiguous and nonoverlapping observations. Additional HST campaigns to capture more flares are risky—even with these observations, LTT 1445A and GJ 486 do not flare as reliably as a younger, truly active stars like AU Mic (Feinstein et al. 2022). What is needed is a space mission with a high-energy monitoring campaign of a large catalog of M dwarfs. Consistent time-sampling of M dwarfs at high energy would allow us to determine the periodic nature of activity on older, quiet stars, as well as tighten constraints on age–activity–rotation relationships for M dwarf stars, which would in turn provide the most accurate stellar ages we are likely to get for these long-lived low-mass stars.

There are proposed missions to monitor large samples of stars, including M dwarfs, in the X-ray (Advanced X-ray Imaging Satellite, or AXIS; Corrales et al. 2023) and the EUV (Extreme-ultraviolet Stellar Characterization for Atmospheric Physics and Evolution, or ESCAPE; France et al. 2022). The ESCAPE mission in particular has the goal of EUV monitoring for a sample of M dwarfs with direct application to understanding terrestrial exoplanet atmospheres and the impacts of stellar variability on those atmospheres. The impact of M dwarf activity on observations of terrestrial exoplanets is becoming increasingly important in the JWST era due to stellar contamination of transmission spectra (e.g., Lustig-Yaeger et al. 2023; Moran et al. 2023; May et al. 2023; Lim et al. 2023). It will take a statistical monitoring survey of M dwarfs at high-energy to push our understanding M dwarf activity periodicity, ages, and impact on terrestrial exoplanet atmospheres to the point where we can eventually answer questions of exoplanet habitability.

7. Conclusions

In this work, we combine data from HST/COS and STIS (GO Programs 16722 and 16701), *XMM-Newton* (ObsID 23377), and *Chandra* (ObsIDs 23377, 27882, 26210, 27799, 27942), as well as interpolated BT-Settl (CIFIST) models to produce self-consistent panchromatic spectra of LTT 1445A and GJ 486 from 1 Å–20 μm. To fill in an observational gap at EUV wavelengths, we use the DEM method to estimate EUV flux (Duvvuri et al. 2021), and we use the wings of the Ly α line to reconstruct the full profile (Youngblood et al. 2016).

Both LTT 1445A and GJ 486 are considered inactive based on the long rotation periods and optical activity indicators, but

we detect flares in both stars at UV and X-ray wavelengths, suggesting a flare frequency rate that is higher than predicted for inactive stars. The flare frequency distribution we derive from the two UV flares detected from GJ 486 based on their equivalent durations is approximately ten times larger than the larger population of active and inactive M dwarfs (Lloyd et al. 2018), despite the fact that this star is optically quiet (Trifonov et al. 2021). The high-energy activity we see in both M dwarfs, despite a lack of activity from optical indicators, is in line with the conclusions of previous works showing that optical observations fail to predict high-energy activity (Lloyd et al. 2018; Jackman et al. 2024). We consider that this high-energy activity is variable, and may not be captured in a single measurement. A lack of high-energy monitoring of M dwarfs is therefore preventing us from obtaining a comprehensive view of M dwarf activity. We do not know whether the high-energy activity we observe is periodic or sporadic. Only taking snapshots of stars at high energy will also contaminate age–activity relations, which are some of the best ways to constrain M dwarf ages (Wright & Drake 2016; Engle 2024).

Variable high-energy activity will also affect our interpretation of planetary atmospheres. LTT 1445Ab, LTT 1445Ac, and GJ 486b have lost any primordial hydrogen-dominated atmospheres they may have had, but higher mean-molecular-weight secondary atmospheres are still possible. Efforts to determine the atmospheric status of a sample of terrestrial exoplanets orbiting M dwarfs is underway (e.g., the Hot Rocks Survey, JWST GO Program 3730; PI H. Diamond-Lowe, Co-PI J. M. Mendonça), with a top recommendation by the Working Group on Strategic Exoplanet Initiatives with HST and JWST to “understand the prevalence and diversity of atmospheres on rocky-M dwarf worlds” (Redfield et al. 2024). As noted by the working group report, detecting and characterizing terrestrial exoplanet atmospheres must go side by side with characterizing their M dwarf hosts. Measuring and monitoring high-energy flux from M dwarfs is the next step toward determining the ages, mass-loss rates, and activity cycles of these key exoplanet hosts.

Acknowledgements. This paper includes data gathered with the Cosmic Origins Spectrograph and the Space Telescope Imaging Spectrograph on board the *Hubble Space Telescope*. This research has used data obtained by the *Chandra X-ray Observatory* and software provided by the *Chandra X-ray Center* (CXC) in the CIAO application package. We make use of the CHIANTI database and open-source python code. CHIANTI is a collaborative project involving George Mason University, University of Michigan (USA), University of Cambridge (UK), and NASA Goddard Space Flight Center (USA). This publication makes use of VOSA, developed under the Spanish Virtual Observatory (<https://svo.cab.inta-csic.es>) project funded by MCIN/AEI/10.13039/501100011033/ through grant PID2020-112949GB-I00. VOSA has been partially updated by using funding from the European Union’s Horizon 2020 Research and Innovation Programme, under Grant Agreement no. 776403 (EXOPLANETS-A). This work has made use of data from the European Space Agency (ESA) mission *Gaia* (<https://www.cosmos.esa.int/gaia>), processed by the *Gaia* Data Processing and Analysis Consortium (DPAC, <https://www.cosmos.esa.int/web/gaia/dpac/consortium>). Funding for the DPAC has been provided by national institutions, in particular the institutions participating in the *Gaia* Multilateral Agreement. This job has made use of the Python package *GaiaXP*, developed and maintained by members of the *Gaia* Data Processing and Analysis Consortium (DPAC), and in particular, Coordination Unit 5 (CU5), and the Data Processing Centre located at the Institute of Astronomy, Cambridge, UK (DPCI). We thank Thea Kozakis for participation in the proposal for GO Program 16722, and Daria Kubyshkina for a helpful discussion of hydrodynamic mass loss. We thank the anonymous referee for their comments, which led to improvements in this paper. H.D.-L. acknowledges support from the Carlsberg Foundation, grant CF22-1254. G.W.K. and L.C. acknowledge support through NASA grant HST-GO-16722-002-A. A.Y. acknowledges support through NASA grant HST-GO-16701.001-A administered by Space Telescope Science Institute. A.B. acknowledges *Chandra* grants GO1-22005X and GO2-23002X to the University of Colorado. Y.M. acknowledges funding from the European Research Council

(ERC) under the European Union's Horizon 2020 research and innovation programme (grant agreement no. 101088557, N-GINE). C.S. acknowledges grant DLR 50 OR 2205.

Facilities used in this work are: HST (STIS, COS); CXO (ACIS, HRI); XMM-Newton (EPIC).

Software used in this work: astropy (Price-Whelan et al. 2018); CIAO (Fruscione et al. 2006); *dyneisty* (Speagle 2020); *emcee* (Foreman-Mackey et al. 2013); *lmfit* (Newville et al. 2016); XSPEC (Arnaud 1996)

References

- Agol, E., Dorn, C., Grimm, S. L., et al. 2021, *Planetary Science Journal*, 2, 1
- Allard, F., Allard, N. F., Homeier, D., et al. 2007, *A&A*, 474, L21
- Allard, F., Guillot, T., Ludwig, H.-G., et al. 2003, in *Brown Dwarfs*, ed. E. Martín, Vol. 211, 325
- Allard, F., Homeier, D., & Freytag, B. 2011, in *Astronomical Society of the Pacific Conference Series*, Vol. 448, 16th Cambridge Workshop on Cool Stars, Stellar Systems, and the Sun, ed. C. Johns-Krull, M. K. Browning, & A. A. West, 91
- Allard, F., Homeier, D., & Freytag, B. 2012, *Philosophical Transactions of the Royal Society of London Series A*, 370, 2765
- Allard, F., Homeier, D., Freytag, B., Schaffenberger, W., & Rajpurohit, A. S. 2013, *Memorie della Societa Astronomica Italiana Supplementi*, 24, 128
- Arnaud, K. A. 1996, in *Astronomical Society of the Pacific Conference Series*, Vol. 101, *Astronomical Data Analysis Software and Systems V*, ed. G. H. Jacoby & J. Barnes, 17
- Artigau, É., Kouach, D., Donati, J.-F., et al. 2014, in *Ground-based and Airborne Instrumentation for Astronomy V*, Vol. 9147, 914715
- Astudillo-Defru, N., Delfosse, X., Bonfils, X., et al. 2017, *A&A*, 600, A13
- Barber, R. J., Tennyson, J., Harris, G. J., & Tolchenov, R. N. 2006, *MNRAS*, 368, 1087
- Barnes, S. A. 2003, *ApJ*, 586, L145
- Bayo, A., Rodrigo, C., Barrado Y Navascués, D., et al. 2008, *A&A*, 492, 277
- Berger, V. L., Hinkle, J. T., Tucker, M. A., et al. 2023, *arXiv e-prints*, arXiv:2312.12511
- Bonfils, X., Mayor, M., Delfosse, X., et al. 2007, *A&A*, 474, 293
- Borucki, W. J., Koch, D., Basri, G., et al. 2010, *Science*, 327, 977
- Bouchy, F., Doyon, R., Artigau, É., et al. 2017, *The Messenger*, 169, 21
- Bourrier, V., Ehrenreich, D., Lecavelier des Etangs, A., et al. 2018, *A&A*, 615, A117
- Brown, A., Froning, C. S., Youngblood, A., et al. 2022, *AJ*, 164, 206
- Brown, A., Schneider, P. C., France, K., et al. 2023, *AJ*, 165, 195
- Caballero, J. A., González-Álvarez, E., Brady, M., et al. 2022, *A&A*, 665, A120
- Caffau, E., Ludwig, H. G., Steffen, M., Freytag, B., & Bonifacio, P. 2011, *Sol. Phys.*, 268, 255
- Cash, W. 1979, *ApJ*, 228, 939
- Catling, D. C. & Kasting, J. F. 2017, *Atmospheric Evolution on Inhabited and Lifeless Worlds*
- Chen, H., Zhan, Z., Youngblood, A., et al. 2021, *Nature Astronomy*, 5, 298
- Choi, J., Dotter, A., Conroy, C., et al. 2016, *ApJ*, 823, 102
- Ciesla, F. J., Mulders, G. D., Pascucci, I., & Apai, D. 2015, *ApJ*, 804, 9
- Cohen, O., Ma, Y., Drake, J. J., et al. 2015, *ApJ*, 806, 41
- Corrales, L., Stassun, K. G., Cunningham, T., et al. 2023, *arXiv e-prints*, arXiv:2311.07674
- Cosentino, R., Lovis, C., Pepe, F., et al. 2012, in *Society of Photo-Optical Instrumentation Engineers (SPIE) Conference Series*, Vol. 8446, *Proc. SPIE*, 84461V
- Craig, N., Abbott, M., Finley, D., et al. 1997, *ApJS*, 113, 131
- Crossfield, I. J. M., Malik, M., Hill, M. L., et al. 2022, *ApJ*, 937, L17
- Cruz Aguirre, F., Youngblood, A., France, K., & Bourrier, V. 2023, *ApJ*, 946, 98
- Davenport, J. R. A., Hawley, S. L., Hebb, L., et al. 2014, *ApJ*, 797, 122
- Del Zanna, G., Landini, M., & Mason, H. E. 2002, *A&A*, 385, 968
- Dere, K. P., Del Zanna, G., Young, P. R., & Landi, E. 2023, *ApJS*, 268, 52
- Dere, K. P., Landi, E., Mason, H. E., Monsignor Fossi, B. C., & Young, P. R. 1997, *A&AS*, 125, 149
- Diamond-Lowe, H., Kreidberg, L., Harman, C. E., et al. 2022, *AJ*, 164, 172
- Diamond-Lowe, H., Mendonça, J. M., Charbonneau, D., & Buchhave, L. A. 2023, *AJ*, 165, 169
- Diamond-Lowe, H., Youngblood, A., Charbonneau, D., et al. 2021, *AJ*, 162, 10
- Dong, C., Jin, M., Lingam, M., et al. 2018, *Proceedings of the National Academy of Science*, 115, 260
- Duvvuri, G. M., Cauley, P. W., Aguirre, F. C., et al. 2023, *AJ*, 166, 196
- Duvvuri, G. M., Sebastian Pineda, J., Berta-Thompson, Z. K., et al. 2021, *ApJ*, 913, 40
- Eastman, J. D., Diamond-Lowe, H., & Tayar, J. 2023, *AJ*, 166, 132
- Engle, S. G. 2024, *ApJ*, 960, 62
- Engle, S. G. & Guinan, E. F. 2023, *ApJ*, 954, L50
- Feinstein, A. D., France, K., Youngblood, A., et al. 2022, *AJ*, 164, 110
- Feldman, P. D., Sahnou, D. J., Kruk, J. W., Murphy, E. M., & Moos, H. W. 2001, *J. Geophys. Res.*, 106, 8119
- Foley, B. J. & Smye, A. J. 2018, *Astrobiology*, 18, 873
- Fontenla, J. M., Linsky, J. L., Garrison, J., et al. 2016, *ApJ*, 830, 154
- Foreman-Mackey, D., Hogg, D. W., Lang, D., & Goodman, J. 2013, *PASP*, 125, 306
- France, K., Arulanantham, N., Fossati, L., et al. 2018, *ApJS*, 239, 16
- France, K., Duvvuri, G., Egan, H., et al. 2020, *AJ*, 160, 237
- France, K., Fleming, B., Youngblood, A., et al. 2022, *Journal of Astronomical Telescopes, Instruments, and Systems*, 8, 014006
- France, K., Loyd, R. O. P., Youngblood, A., et al. 2016, *ApJ*, 820, 89
- Fressin, F., Torres, G., Charbonneau, D., et al. 2013, *ApJ*, 766, 81
- Froning, C. S., Kowalski, A., France, K., et al. 2019, *ApJ*, 871, L26
- Fruscione, A., McDowell, J. C., Allen, G. E., et al. 2006, in *Society of Photo-Optical Instrumentation Engineers (SPIE) Conference Series*, Vol. 6270, *Observatory Operations: Strategies, Processes, and Systems*, ed. D. R. Silva & R. E. Doxsey, 62701V
- Fuhrmeister, B., Zisik, A., Schneider, P. C., et al. 2022, *A&A*, 663, A119
- Fulton, B. J., Pettigura, E. A., Howard, A. W., et al. 2017, *AJ*, 154, 109
- Gaia Collaboration, Prusti, T., de Bruijne, J. H. J., et al. 2016, *A&A*, 595, A1
- Gaia Collaboration, Vallenari, A., Brown, A. G. A., et al. 2023, *A&A*, 674, A1
- Garraffo, C., Drake, J. J., & Cohen, O. 2016, *ApJ*, 833, L4
- Garraffo, C., Drake, J. J., Cohen, O., Alvarado-Gómez, J. D., & Moschou, S. P. 2017, *ApJ*, 843, L33
- Gillmann, C., Chassefière, E., & Lognonné, P. 2009, *Earth and Planetary Science Letters*, 286, 503
- Gillon, M., Jehin, E., Fumel, A., Magain, P., & Queloz, D. 2013, in *European Physical Journal Web of Conferences*, Vol. 47
- Ginsburg, A. & Mirocha, J. 2011, *PySpecKit: Python Spectroscopic Toolkit, Astrophysics Source Code Library*, record ascl:1109.001
- Ginsburg, A., Sokolov, V., de Val-Borro, M., et al. 2022, *AJ*, 163, 291
- Gordiets, B. F. & Kulikov, Y. N. 1985, *Advances in Space Research*, 5, 113
- Greene, T. P., Bell, T. J., Ducrot, E., et al. 2023, *Nature*, 618, 39
- Gregory, P. C. & Loredro, T. J. 1992, *ApJ*, 398, 146
- Harman, C. E., Schwieterman, E. W., Schottelkotte, J. C., & Kasting, J. F. 2015, *ApJ*, 812, 137
- Hawley, S. L., Davenport, J. R. A., Kowalski, A. F., et al. 2014, *ApJ*, 797, 121
- Hawley, S. L. & Pettersen, B. R. 1991, *ApJ*, 378, 725
- Hojjatpanah, S., Figueira, P., Santos, N. C., et al. 2019, *A&A*, 629, A80
- Howard, W. S., Kowalski, A. F., Flagg, L., et al. 2023, *ApJ*, 959, 64
- Howard, W. S. & Law, N. M. 2021, *ApJ*, 920, 42
- Husser, T. O., Wende-von Berg, S., Dreizler, S., et al. 2013, *A&A*, 553, A6
- Irwin, J. M., Berta-Thompson, Z. K., Charbonneau, D., et al. 2015, in *Cambridge Workshop on Cool Stars, Stellar Systems, and the Sun*, Vol. 18, 18th Cambridge Workshop on Cool Stars, Stellar Systems, and the Sun, 767–772
- Iyer, A. R., Line, M. R., Muirhead, P. S., Fortney, J. J., & Gharib-Nezhad, E. 2023, *ApJ*, 944, 41
- Jackman, J. A. G., Shkolnik, E. L., Loyd, R. O. P., & Richey-Yowell, T. 2024, *arXiv e-prints*, arXiv:2406.15308
- Jackman, J. A. G., Shkolnik, E. L., Million, C., et al. 2023, *MNRAS*, 519, 3564
- Jackman, J. A. G., Wheatley, P. J., Bayliss, D., et al. 2019, *MNRAS*, 485, L136
- Jackman, J. A. G., Wheatley, P. J., Pugh, C. E., et al. 2018, *MNRAS*, 477, 4655
- Johnstone, C. P., Lammer, H., Kislyakova, K. G., Scherf, M., & Güdel, M. 2021, *Earth and Planetary Science Letters*, 576, 117197
- Kashyap, V. & Drake, J. J. 1998, *ApJ*, 503, 450
- King, G. W. & Wheatley, P. J. 2021, *MNRAS*, 501, L28
- Kowalski, A. F., Hawley, S. L., Wisniewski, J. P., et al. 2013, *ApJS*, 207, 15
- Kreidberg, L., Koll, D. B., Morley, C., et al. 2019, *Nature*, 573, 87
- Kubyshkina, D. 2024, *arXiv e-prints*, arXiv:2402.13931
- Kubyshkina, D. & Vidotto, A. A. 2021, *MNRAS*, 504, 2034
- Lammer, H., Zerkle, A. L., Gebauer, S., et al. 2018, *Astronomy and Astrophysics Review*, 26, 2
- Lim, O., Benneke, B., Doyon, R., et al. 2023, *ApJ*, 955, L22
- Linsky, J. L., Fontenla, J., & France, K. 2014, *ApJ*, 780, 61
- Lopez, E. D. & Fortney, J. J. 2013, *ApJ*, 776, 2
- Lopez, E. D., Fortney, J. J., & Miller, N. 2012, *ApJ*, 761, 59
- Louca, A. J., Miguel, Y., Tsai, S.-M., et al. 2023, *MNRAS*, 521, 3333
- Loyd, R. O. P. & France, K. 2014, *ApJS*, 211, 9
- Loyd, R. O. P., France, K., Youngblood, A., et al. 2016, *ApJ*, 824, 102
- Loyd, R. O. P., France, K., Youngblood, A., et al. 2018, *ApJ*, 867, 71
- Loyd, R. O. P., Shkolnik, E. L., France, K., Wood, B. E., & Youngblood, A. 2020, *Research Notes of the American Astronomical Society*, 4, 119
- Luger, R. & Barnes, R. 2015, *Astrobiology*, 15, 119
- Luger, R., Barnes, R., Lopez, E., et al. 2015, *Astrobiology*, 15, 57
- Lustig-Yaeger, J., Fu, G., May, E. M., et al. 2023, *Nature Astronomy*, 7, 1317
- MacGregor, M. A., Weinberger, A. J., Loyd, R. O. P., et al. 2021, *ApJ*, 911, L25
- Mahadevan, S., Ramsey, L., Wright, J., et al. 2010, in *Proc. SPIE*, Vol. 7735, *Ground-based and Airborne Instrumentation for Astronomy III*, 77356X
- Marty, B. & Dauphas, N. 2003, *Earth and Planetary Science Letters*, 206, 397

- May, E. M., MacDonald, R. J., Bennett, K. A., et al. 2023, *ApJ*, 959, L9
- Mayor, M., Pepe, F., Queloz, D., et al. 2003, *The Messenger*, 114, 20
- Medina, A. A., Winters, J. G., Irwin, J. M., & Charbonneau, D. 2022, *ApJ*, 935, 104
- Melbourne, K., Youngblood, A., France, K., et al. 2020, *AJ*, 160, 269
- Moran, S. E., Stevenson, K. B., Sing, D. K., et al. 2023, *ApJ*, 948, L11
- Newton, E. R., Irwin, J., Charbonneau, D., et al. 2017, *ApJ*, 834, 85
- Newton, E. R., Irwin, J., Charbonneau, D., et al. 2016, *ApJ*, 821, 93
- Newton, E. R., Mondrik, N., Irwin, J., Winters, J. G., & Charbonneau, D. 2018, *AJ*, 156, 217
- Newville, M., Stensitzki, T., Allen, D. B., et al. 2016, *Lmfit: Non-Linear Least-Square Minimization and Curve-Fitting for Python*
- Nutzman, P. & Charbonneau, D. 2008, *PASP*, 120, 317
- O'Brien, D. P., Izidoro, A., Jacobson, S. A., Raymond, S. N., & Rubie, D. C. 2018, *Space Sci. Rev.*, 214, 47
- Odert, P., Lammer, H., Erkaev, N. V., et al. 2018, *Icarus*, 307, 327
- Owen, J. E., Shaikhislamov, I. F., Lammer, H., Fossati, L., & Khodachenko, M. L. 2020, *Space Sci. Rev.*, 216, 129
- Owen, J. E. & Wu, Y. 2013, *ApJ*, 775, 105
- Owen, J. E. & Wu, Y. 2017, *ApJ*, 847, 29
- Passegger, V. M., Schweitzer, A., Shulyak, D., et al. 2019, *A&A*, 627, A161
- Pepin, R. O. 1991, *Icarus*, 92, 2
- Pineda, J. S., Youngblood, A., & France, K. 2021, *ApJ*, 918, 40
- Price-Whelan, A. M., Sipőcz, B. M., Günther, H. M., et al. 2018, *AJ*, 156, 123
- Pye, J. P., Rosen, S., Fyfe, D., & Schröder, A. C. 2015, *A&A*, 581, A28
- Quirrenbach, A., Amado, P. J., Mandel, H., et al. 2010, in *Proc. SPIE*, Vol. 7735, Ground-based and Airborne Instrumentation for Astronomy III, 773513
- Raymond, S. N., Scalo, J., & Meadows, V. S. 2007, *ApJ*, 669, 606
- Reale, F., Peres, G., & Orlando, S. 2001, *ApJ*, 557, 906
- Redfield, S., Batalha, N., Benneke, B., et al. 2024, *arXiv e-prints*, arXiv:2404.02932
- Ricker, G. R., Winn, J. N., Vanderspek, R., et al. 2015, *Journal of Astronomical Telescopes, Instruments, and Systems*, 1, 014003
- Ridden-Harper, A., Nugroho, S. K., Flagg, L., et al. 2023, *AJ*, 165, 170
- Rugheimer, S., Kaltenegger, L., Segura, A., Linsky, J., & Mohanty, S. 2015, *ApJ*, 809, 57
- Sanz-Forcada, J., Brickhouse, N. S., & Dupree, A. K. 2003, *ApJS*, 145, 147
- Schatzman, E. 1962, *Annales d'Astrophysique*, 25, 18
- Schwab, C., Rakich, A., Gong, Q., et al. 2016, in *Proc. SPIE*, Vol. 9908, Ground-based and Airborne Instrumentation for Astronomy VI, 99087H
- Seager, S. & Deming, D. 2010, *ARA&A*, 48, 631
- Segura, A., Walkowicz, L. M., Meadows, V., Kasting, J., & Hawley, S. 2010, *Astrobiology*, 10, 751
- Seifahrt, A., Bean, J. L., Stürmer, J., et al. 2016, in *Proc. SPIE*, Vol. 9908, Ground-based and Airborne Instrumentation for Astronomy VI, 990818
- Skumanich, A. 1972, *ApJ*, 171, 565
- Sleep, N. H. & Zahnle, K. 2001, *J. Geophys. Res.*, 106, 1373
- Speagle, J. S. 2020, *MNRAS*, 493, 3132
- Teal, D. J., Kempton, E. M. R., Bastelberger, S., Youngblood, A., & Arney, G. 2022, *ApJ*, 927, 90
- Teixeira, K. E., Morley, C. V., Foley, B. J., & Unterborn, C. T. 2024, *ApJ*, 960, 44
- Tian, F., France, K., Linsky, J. L., Mauas, P. J. D., & Vieytes, M. C. 2014, *Earth and Planetary Science Letters*, 385, 22
- Tovar Mendoza, G., Davenport, J. R. A., Agol, E., Jackman, J. A. G., & Hawley, S. L. 2022, *AJ*, 164, 17
- Trifonov, T., Caballero, J. A., Morales, J. C., et al. 2021, *Science*, 371, 1038
- Tsai, S.-M., Lee, E. K. H., Powell, D., et al. 2023, *Nature*, 617, 483
- Van Looveren, G., Güdel, M., Boro Saikia, S., & Kislyakova, K. 2024, *A&A*, 683, A153
- Walsh, B. M., Kuntz, K. D., Collier, M. R., et al. 2014, *Space Weather*, 12, 387
- Wilson, D. J., Froning, C. S., Duvvuri, G. M., et al. 2021, *ApJ*, 911, 18
- Winters, J. G., Cloutier, R., Medina, A. A., et al. 2022, *AJ*, 163, 168
- Winters, J. G., Medina, A. A., Irwin, J. M., et al. 2019, *AJ*, 158, 152
- Wood, B. E., Müller, H.-R., Redfield, S., et al. 2021, *ApJ*, 915, 37
- Wright, N. J. & Drake, J. J. 2016, *Nature*, 535, 526
- Wright, N. J., Newton, E. R., Williams, P. K. G., Drake, J. J., & Yadav, R. K. 2018, *MNRAS*, 479, 2351
- Youngblood, A., France, K., Loyd, R. O. P., et al. 2017, *ApJ*, 843, 31
- Youngblood, A., France, K., Loyd, R. O. P., et al. 2016, *ApJ*, 824, 101
- Youngblood, A., Pineda, J. S., Ayres, T., et al. 2022, *ApJ*, 926, 129
- Youngblood, A., Pineda, J. S., & France, K. 2021, *ApJ*, 911, 112
- Zahnle, K. J. & Catling, D. C. 2017, *ApJ*, 843, 122
- Zahnle, K. J. & Kasting, J. F. 1986, *Icarus*, 68, 462
- Zhang, M., Hu, R., Inglis, J., et al. 2024, *ApJ*, 961, L44
- Zieba, S., Kreidberg, L., Ducrot, E., et al. 2023, *Nature*, 620, 746